UNIVERSITÀ DEGLI STUDI DI PADOVA

SCUOLA DI SCIENZE
DIPARTIMENTO DI GEOSCIENZE
DIRETTORE PROF. NICOLA SURIAN

MASTER'S DEGREE IN
GEOPHYSICS FOR NATURAL RISKS
AND RESOURCES

DEEP SHEAR WAVES MODEL OF THE VENICE LAGOON FROM SEISMIC NOISE INTERFEROMETRY

Supervisor: Prof. Jacopo Boaga
Co-supervisors: Prof. Piero Poli
Dott.ssa Ilaria Barone

Candidate: Silvia De Marchi
Student number: 2091755

A.Y. 2023/2024

"The secret of life, though, is to fall seven times and to get up eight times."

The Alchemist, Paulo Coelho

Abstract

Seismic noise interferometry is a geophysical technique that transforms passive noise from sources such as human activities, sea waves, wind, and earthquakes into a signal that can be studied to obtain information about the Earth's subsurface. This method involves performing cross-correlation of seismic noise to evaluate surface wave dispersion passively, without the need of active sources.

Cross-correlation of seismic noise recordings can infer the impulse response between two points when the noise correlation function (NCF) converges to the impulse response between two receivers, filtered by the noise spectrum's bandwidth.

In this study, we computed the NCF between two sensors located in the Venice Lagoon, Italy, in San Sèrvolo and Lido islands. The aim was to obtain the first deep velocity model of the Venice lagoon from passive noise, since in this environment traditional controlled source seismic surveys are particularly challenging.

The dispersion curve of the fundamental mode for Rayleigh waves was extracted from the NCF using the Frequency-Time Analysis (FTAN) method. The non-linear inversion of dispersion data, in terms of one-dimensional V_s and V_p distribution versus depth, is consistent with the geological subsoil conditions and it represents the first deep velocity profile of this area of the Venetian lagoon, interesting for shaking models that could affect the historic center of Venice, which is of enormous value in terms of exposure and vulnerability.

Riassunto

L'interferometria del rumore sismico è una tecnica geofisica che trasforma il rumore passivo generato da fonti come attività umane, onde marine, vento e terremoti, in un segnale che può essere studiato per ottenere informazioni sul sottosuolo terrestre. Questo metodo prevede l'esecuzione della correlazione incrociata del rumore per valutare la dispersione delle onde di superficie in modo passivo, senza l'utilizzo di sorgenti attive.

La correlazione incrociata del rumore sismico può inferire la risposta all'impulso tra due punti quando la funzione di correlazione del rumore (NCF) converge alla risposta all'impulso tra due ricevitori, filtrata dalla larghezza di banda dello spettro del rumore.

In questo studio, è stata calcolata la NCF tra due sensori situati nella Laguna di Venezia, Italia, rispettivamente nelle isole di San Sèrvolo e Lido. L'obiettivo era ricavare il primo modello profondo di velocità della laguna veneziana utilizzando il rumore passivo, poiché in questo ambiente i sondaggi sismici tradizionali con sorgenti controllate sono particolarmente difficili da eseguire.

La curva di dispersione del modo fondamentale delle onde di Rayleigh è stata quindi estratta dalla NCF utilizzando il metodo FTAN (Frequency-Time Analysis). L'inversione non lineare dei dati di dispersione, in termini di distribuzione unidimensionale delle V_s e V_p rispetto alla profondità, è coerente con le condizioni geologiche del sottosuolo e rappresenta il primo modello di velocità profondo di quest'area, di particolare interesse per i modelli di scuotimento che potrebbero interessare il centro storico di Venezia, il quale ha un enorme valore in termini di esposizione e vulnerabilità.

Contents

1. Introduction

This chapter will describe in detail what is meant by seismic noise, its main characteristics and the sources that generate it, both natural and anthropogenic. It will also define the fundamental concepts of seismic noise interferometry, a geophysical method used to study the Earth's subsurface structure. Finally, it will be introduced the cross-correlation of seismic signals, which allows to extract the impulsive response of a medium between two receivers.

1.1 Seismic noise interferometry

Unlike the distinct and high-energy waves produced by earthquakes or explosions, seismic noise is typically a background hum that persists continuously. It refers to the continuous, low-amplitude vibrations of the Earth's surface generated by a variety of natural and anthropogenic sources, detectable as a superposition of body waves, surface waves, microseisms, and microtremors. Especially when it includes low-frequency components, seismic noise can provide valuable information about the subsurface, since it continuously propagates through the Earth and can be recorded over long periods, capturing signals from various depths and directions.

Despite its low energy, ambient noise contains valuable information about the subsurface, because it is generated across a wide range of frequencies and it is ubiquitous. The frequency of the ambient noise's wavefield ranges between 1 mHz and 100 Hz (Nishida, 2017). High-frequency noise (f > 1 Hz) is generally due to human activities, such as traffic, industrial operations, machinery, construction. The energy of these type of signals varies with time, since it is correlated with human life rhythms, characterized by daily and weekly periodicity (Campillo and Roux, 2015). On the other hand, low-frequency noise (f < 1 Hz), is associated with the interaction of the oceanic swell, wind waves and ocean infragravity waves with the solid Earth. According to the frequencies of these wavefields, they are categorized into seismic hum (1–20 mHz), and microseisms (0.02-1 Hz), which can be distinguished into primary, with frequencies ranging between 0.02 and 0.1 Hz, and secondary, between 0.1 and 0.5 Hz (Nishida, 2017).

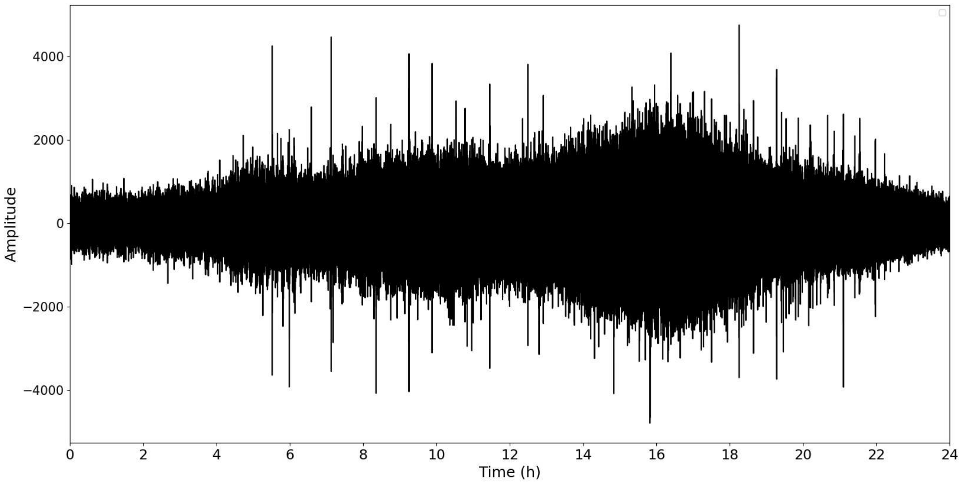

Figure 1: Example of ambient noise recorded in Venice Lido on July 8th, 2023. Each of the high amplitude peaks indicates an increase in seismic motion, and they generally concentrate between 5 a.m. and 10 p.m., when human activity is greater.

Surface waves, especially Rayleigh waves, represent the dominant part in low-frequency seismic noise, making it a valuable resource for seismic investigations aimed at exploring the Earth's subsurface. An example is seismic noise interferometry: without the need for active sources, this method involves the cross-correlation of diffuse seismic noise wavefield, passively and continuously recorded at different receiver locations, in order to estimate inter-receiver wave signals, as if one of the receivers were located at a virtual source. Ambient noise signals recorded at different stations are considered to be uncorrelated, since they result from variable interferences, and cross-correlation methods aim at extracting the coherent part of the signals that contains deterministic information on wave propagation between the two receivers (Campillo and Roux, 2015).

Given the extensive applications of surface waves in subsurface investigations, this thesis specifically focuses on surface-wave transmission responses, which provide critical insights into the medium's properties. In dealing with a diffuse wavefield, all wave modes are present, and their amplitudes are uncorrelated but still have equal expected energies (Wapenaar et al., 2010). Experimental and theoretical studies have demonstrated that the time-averaged cross-correlation of an isotropic random wavefield, computed between two receivers, known as the noise correlation function (NCF), converges into the intersta- tion Green's function, which is the impulsive response of the medium between the two receivers, filtered by the bandwidth of the noise spectrum. In order to derive the NCF from seismic noise, data need to be standardized before performing the cross-correlation. Various data processing strategies, i.e., attenuating amplitudes above a certain threshold

(Bensen et al., 2007), are employed to improve the signal-to-noise ratio. After homogenizing the traces, cross-correlation is performed for multiple time windows, and the results are stacked to enhance the Green's function between the stations.

1.1.1 Cross correlation and Green's function

In signal processing, correlation can be done with only one signal (*autocorrelation*), or between two different signals (*cross-correlation*). Autocorrelation measures the distribution of the energy within a signal, given by the amplitude of a peak at zero lag. Instead, cross-correlation measures the similarity between two series, as function of the displacement of one signal relative to the other, estimating the degree of correlation between them. Cross-correlation is similar in nature to convolution; however, unlike convolution, which involves the time reversal of one signal before shifting and multiplying it with the other, cross-correlation involves only the shift and the product.

Cross-correlation is an integral part of seismic noise interferometry, and it is used to analyze the similarity of noise signals recorded by different receivers. Since the distance between recording stations prevents the waves from reaching each receiver at the same time, the cross-correlation will be very important in delivering the time delay between arrivals of seismic waves at different seismometers. This time delay gives very important information on the propagation of seismic waves and geological structure of the subsurface of the area between the seismic stations.

The cross-correlation of signals recorded at two receiver locations (i.e., x_A and x_B) can estimate the Green's function between them, as if a virtual source was, for instance, at position x_A. The time-averaged cross-correlation function of the wavefield at the two points, x_A and x_B, can be mathematically expressed as:

$$C_{AB}(\tau) = \frac{1}{T}\int_0^T \langle v(\mathbf{x}_A, t+\tau) v(\mathbf{x}_B, t)\rangle \, dt \tag{1.1}$$

In the equation above, T is the time period, τ is the lag time used for the correlation, $v(x_A,t)$ and $v(x_B,t)$ relate to the data continuously recorded at station positions (Snieder and Wapenaar, 2010).

It has been shown that, if noise sources are properly distributed in space and uncorrelated, their average cross-correlation function will return the superposition of the Green's function and its time-reversed counterpart (Snieder and Wapenaar, 2010):

$$[G(\mathbf{x}_A, \mathbf{x}_B, \tau) + G(\mathbf{x}_A, \mathbf{x}_B, -\tau)] * S_s(\tau) = C_{AB}(\tau) \tag{1.2}$$

In the equation above, $G(x_A, x_B, \tau)$ and $G(x_A, x_B, -\tau)$ are the empirical Green's functions (EGF) of the wavefield generated by x_A and received at x_B, and the one generated by x_B and received at x_A after time reversal, respectively; S_s is the autocorrelation of the source wavelet.

The positive and negative parts of the NCF represent the two opposite directions of wave propagation: the positive part is the noise traveling from x_A to x_B, while the negative part the noise traveling from x_B to x_A. When dealing with diffuse noise, the signal in both parts of the NCF should be identical, indicating that noise travels in all directions. However, in real world, this not always happens and sometimes symmetry needs to be achieved. This approach not only improves the signal-to-noise ratio (SNR), but it also ensures a more uniform source distribution, enhancing the overall quality of the seismic data (Boaga et al., 2007). Some researchers, leveraging the spatial reciprocity of the Green's functions (i.e. Bensen et al., 2007), average the positive and negative parts of the NCF, thereby imposing symmetry, enhancing the SNR and effectively combining signals from opposite directions, resulting in a more homogenized source distribution.

1.2 Seismic waves

Seismic noise mainly includes two types of seismic waves: body waves and surface waves. Body waves, which travel through the Earth's interior, can either be longitudinal, known as P-waves (P, primary), or transverse, known as S-waves (S, secondary). Surface waves, which generally represent the predominant component of low-frequency seismic noise, travel along the Earth's surface and can be distinguished into Rayleigh (*R*) and Love (*L*) waves .

1.2.1 Body waves

Body waves propagate through the Earth's interior, transmitting energy from a seismic event, such as an earthquake, an explosion, or a mechanical disturbance, through the subsurface. They can be distinguished into P-waves and S-waves, depending on the direction of particle motion relative to the direction of wave propagation.

P-waves (P, primary) are compressional (longitudinal) waves, and involve alternating compressions and dilations that move in the direction of wave propagation, which is perpendicular to the wavefront (*Figure 2*). P-waves are the fastest ones, making them the first-arriving energy on a seismogram (*Figure 4*), and they can travel through solids, liquids and gases.

S-waves (S, secondary) are shear (transverse) waves, in which the particles move perpendicular to the direction of wave propagation (*Figure 3*). Their motion is often polarized, such that particle movement occurs in vertical (SV-waves) or horizontal planes (SH-waves). Unlike P-waves, they cannot travel through fluids and have a lower velocity, which is why they appear as secondary arrivals on a seismogram (*Figure 4*).

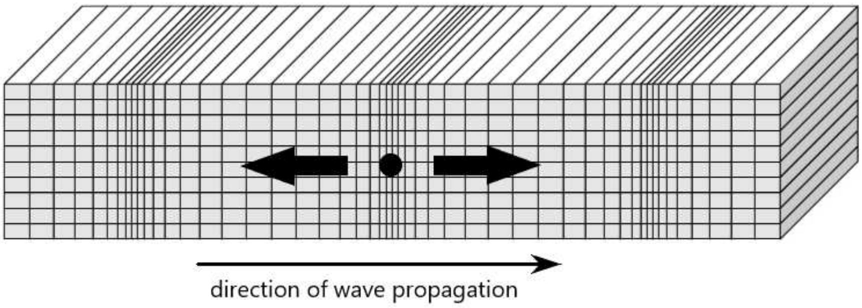

Figure 2: Particle motion in P-waves - modified from Shearer (2009).

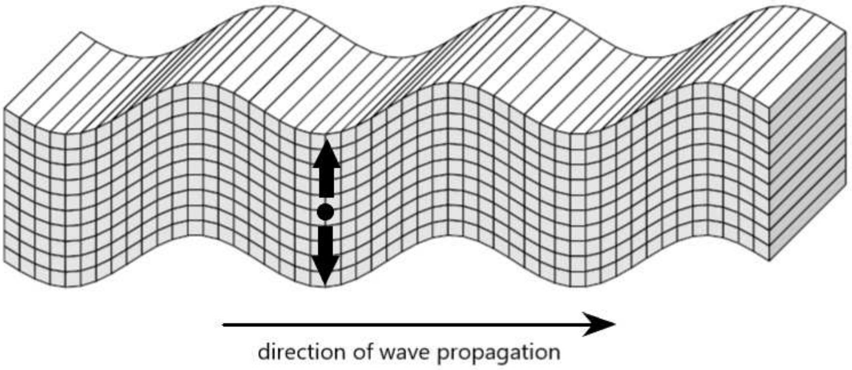

Figure 3: Particle motion in S-waves - modified from Shearer (2009).

The propagation velocity of body waves is governed by the density (ρ) of the material they propagate through and its elastic properties, described by its Lamé constants. The first Lamé constant, λ, is related to the material's resistance to uniform compression, while the second parameter, μ, known as the shear modulus, describes the material's resistance to shear deformation, therefore its rigidity. The velocity of compressional waves (V_p) depends on λ, μ and ρ, making it sensitive to both the material's compressibility and rigidity. In contrast, the velocity of shear waves (V_s) only depends on μ and ρ. Fluids have zero shear modulus, this is why shear waves cannot propagate through them.

Compressional and shear wave velocities can be defined by the following equations:

$$\begin{cases} v_p = \sqrt{\frac{\lambda+2\mu}{\rho}} \\ v_s = \sqrt{\frac{\mu}{\rho}} \end{cases} \tag{1.3}$$

The ratio between P-wave and S-wave velocities can be approximated to $\sqrt{3}$ for a specific material known as a Poisson solid, which is characterized by a Poisson's ratio (ν) of 0.25. The Poisson's ratio is a measure of a material's elasticity and defines the ratio of transverse contraction (or expansion) strain to longitudinal extension strain in the direction of the stretching force. For a Poisson solid, the value of ν is 0.25, which implies that the first Lamé constant (λ) is equal to the shear modulus (μ). Substituting this relationship into the equations for V_p and V_s, the ratio $\frac{V_p}{V_s}$ becomes equal to $\sqrt{3}$. For most rocks, the Poisson's ratio usually ranges between 0.05 and 0.50, depending on their mineral composition, porosity, confining pressure, temperature, state of fracturing, and fluid saturation.

1.2.2 Surface waves

Surface waves are primarily generated when vertically-polarized S-waves and P-waves reach the surface, but they are generally characterized by longer wavelengths and lower frequencies compared to body waves.

Unlike body waves, which travel through the Earth's interior (in three dimensions), surface waves propagate along its surface (in two dimensions), therefore they experience less energy attenuation and maintain their amplitude over longer distances, making them easier to detect in noise records compared to body waves, primarily due to the geometrical effect of wave spreading. Also, in seismic records of distant earthquakes (*teleseisms*), the waves with the greatest amplitudes are in fact surface waves (*Figure 4*). An exception to this is seen in seismograms of deep-focus earthquakes, where body waves are more prominent.

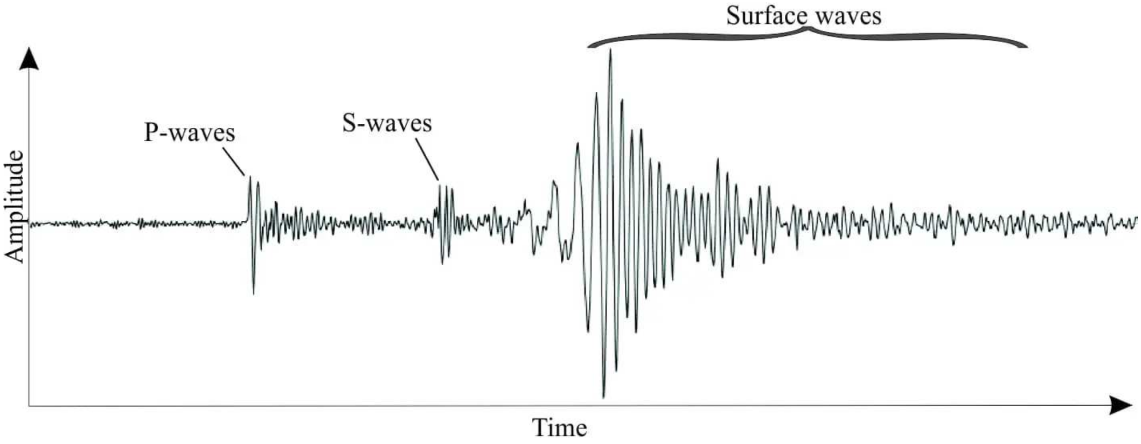

Figure 4: Example of a seismogram highlighting distinguished arrival times for different types of seismic waves - from www.geological-digressions.com.

Since the energy of a surface wave is mostly concentrated near the surface, its displacement field decreases exponentially in the direction orthogonal to that of propagation (Foti et al., 2014). Moreover, most of the strain energy carried by surface waves is limited within a depth of about one wavelength from the surface (Achenbach, 2012). This is why surface waves with long wavelengths can reach greater depths. Since the wavelength is proportional to the inverse of frequency in harmonic waves, it can be said that high-frequency waves are limited to shallow depths, while low-frequency ones can penetrate deeper (Foti et al., 2014).

Another characteristic of surface waves is that, in vertically heterogeneous media, they are dispersive, meaning their phase velocities are frequency-dependent. Dispersion causes different frequency components of a wave packet to travel at different velocities, resulting in a group velocity, the speed of the energy carried by the wave packet (or envelope), that differs from the phase velocity. Group velocities are more affected by depth, and measurements errors are usually a bit larger than those of phase velocities. However, source effects on group velocities are smaller, and therefore usually ignored. The main advantage is that details on earthquake source processes do not have to be known to measure group velocities (Laske, G., Widmer-Schnidrig, R., 2015).

Depending on their particle motion, surface waves can be distinguished into Love and Rayleigh waves. Love waves (*Figure 5*) move parallel to the Earth's surface and perpendicular to the direction of propagation, while Rayleigh waves (*Figure 6*) are a somehow more complex, since they induce an elliptical retrograde motion, as a result of the superposition of vertical and horizontal (radial) components. Most of the shaking felt from an earthquake is due to Rayleigh waves, which can be much larger than that caused by other waves. Like Love waves, the amplitude of these waves decreases dramatically with depth.

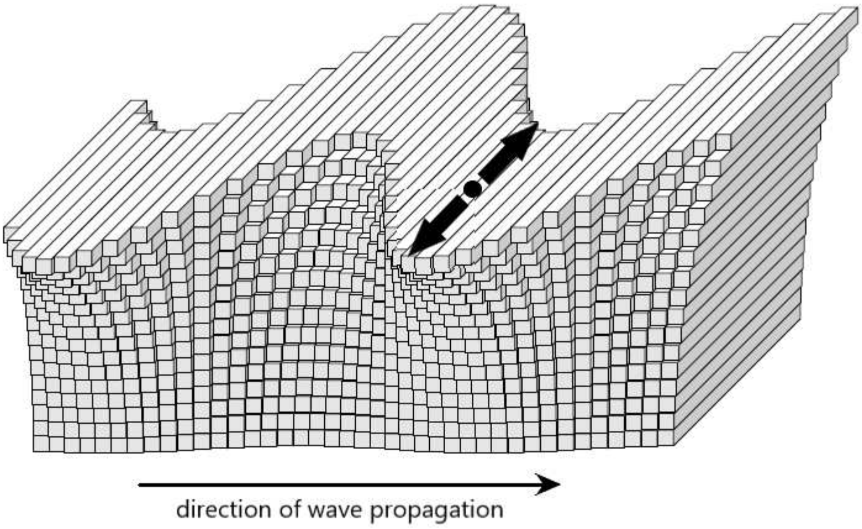

Figure 5: Particle motion in Love waves - modified from Shearer (2009).

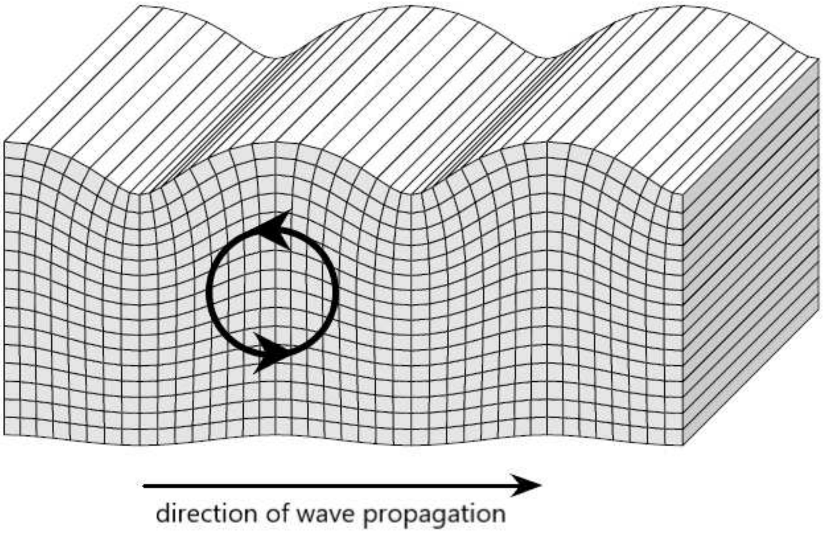

Figure 6: Particle motion in Rayleigh waves - modified from Shearer (2009).

In this work, all surface waves components were initially cross-correlated: vertical (Z), radial (R), and transverse (T). This includes all their combinations: ZZ (vertical-vertical), RR (radial-radial), TT (transverse-transverse), ZR (vertical-radial), ZT (vertical-transverse) and RT (radial-transverse). Each component can provide specific information about different types of seismic waves. For example, TT and RR components are often associated with Love waves, while ZZ and ZR components to Rayleigh waves. Therefore, since the aim was to estimate the fundamental mode for Rayleigh waves, this thesis focused on processing and analyzing only the ZZ component. By studying the dispersion of Rayleigh waves, it was possible to indirectly retrieve a shear wave velocity profile of the subsurface (from which also the compressional wave velocities distribution could be derived).

1.3 Objectives of the thesis

The primary objective of this thesis was to process passively recorded seismic noise to infer the first deep shear wave velocity profile in the challenging environment of the lagoon between San Sèrvolo and Lido islands, interesting for shaking models that could affect the historic center of Venice, which is of enormous value in terms of exposure and vulnerability.

The secondary objective was to study the behavior of the signal-to-noise ratio (SNR) based on the number of weeks of data stacked, verifying how stacking over progressively longer periods tends to enhance the quality of the signal, already demonstrated by Bensen et al., 2007. Moreover, the SNR was measured before and after the application of a spectral whitening, to verify for its effectiveness.

2. Study Area

In this chapter the geological context of the study area will be examined. The main geological elements that characterize the Venice lagoon will be described, including its stratigraphy and the geological processes that have shaped the landscape over time. Finally, the geographical locations of the seismic stations used for noise recording will be given, along with details on the types of instruments employed.

2.1 Geological settings

The Venice Lagoon, the largest in the Mediterranean, is approximately 50 km long, with an average width of 8–15 km (Frascari, 2014). It is situated at the center of the Neogene-Quaternary foreland basin, between the northeast-verging Northern Apennines chain and the southeast-verging Eastern Southern Alps. In a broader regional context, it lies at the northeastern edge of the Adriatic microplate, where the subsurface of the circum-Venetian region and its offshore areas have recorded a long history of sedimentary, magmatic, and tectonic events (Tosi L. et al., 2007). According to the depositional system framework of the Veneto-Friulian Plain, this area is positioned between coastal and deltaic systems, characterized by shallow marine and lagoonal environments, where predominantly medium to fine sediments (sands, silts, and clays) emerge, related to the distal part of the Holocene Brenta megafan. The lagoon morphology includes shallows, tidal flats, salt marshes, islands, and a network of channels. Its boundaries also include fishponds, reclaimed areas, and the coast, which is interrupted by three inlets—Lido, Malamocco, and Chioggia—that allow water exchange with the sea (Brambati et al., 2003).

The geological structure of the Venetian Plain, down to a depth of 5,000 meters, consists of Pre-Pliocene, Pliocene, and Quaternary deposits. The thickness of Quaternary sediments varies significantly, from about 3,000 meters in the southern region to a few hundred meters in the northern region. These sediments are mainly composed of sandy and silty-clayey layers formed through alluvial and marine processes (Brambati et al., 2003).

In 1971, in response to the alarm about the accelerated subsidence of Venice in the 1960s, the biostratigraphic and chronostratigraphic knowledge of the deep deposits in the Venetian area was expanded through the drilling of two deep boreholes, VE-1 (949.7 m) and VE-1bis (120.3 m), conducted by the Consiglio Nazionale delle Ricerche (CNR) of Italy in Isola Nuova del Tronchetto (inner lagoon). More recently, the Pleistocene stratigraphic sequence has been updated by Kent et al. (2002) and Massari et al. (2004).

Core samples from VE-1 and VE-1bis (*Figure 7*) revealed an alternation of gravel, sandy gravel, sand, interlaminated silt/fine sand, clay, marine marl and mudstone with occasional bioturbation and sapropel layers, especially around 785 m. At 815 m, after the sapropel bundles, the shelf to shoreface succession begins, with thicker layers of shelly sand, marine marl and mudstone, with no more presence of finely interlaminated silt/fine sand/clay (*Figure 8*). Moreover, there is a particular concentration of turbidites around 800 m, while layers of gravel and sandy gravel mainly concentrate in the first 300 m.

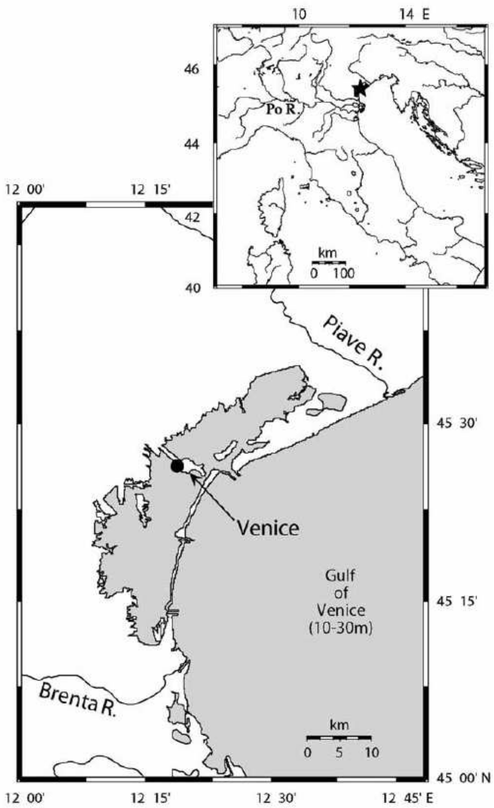

Figure 7: Map of Venice lagoon and location of the CNR cores Venice 1 and Venice 1bis (Massari et al., 2004).

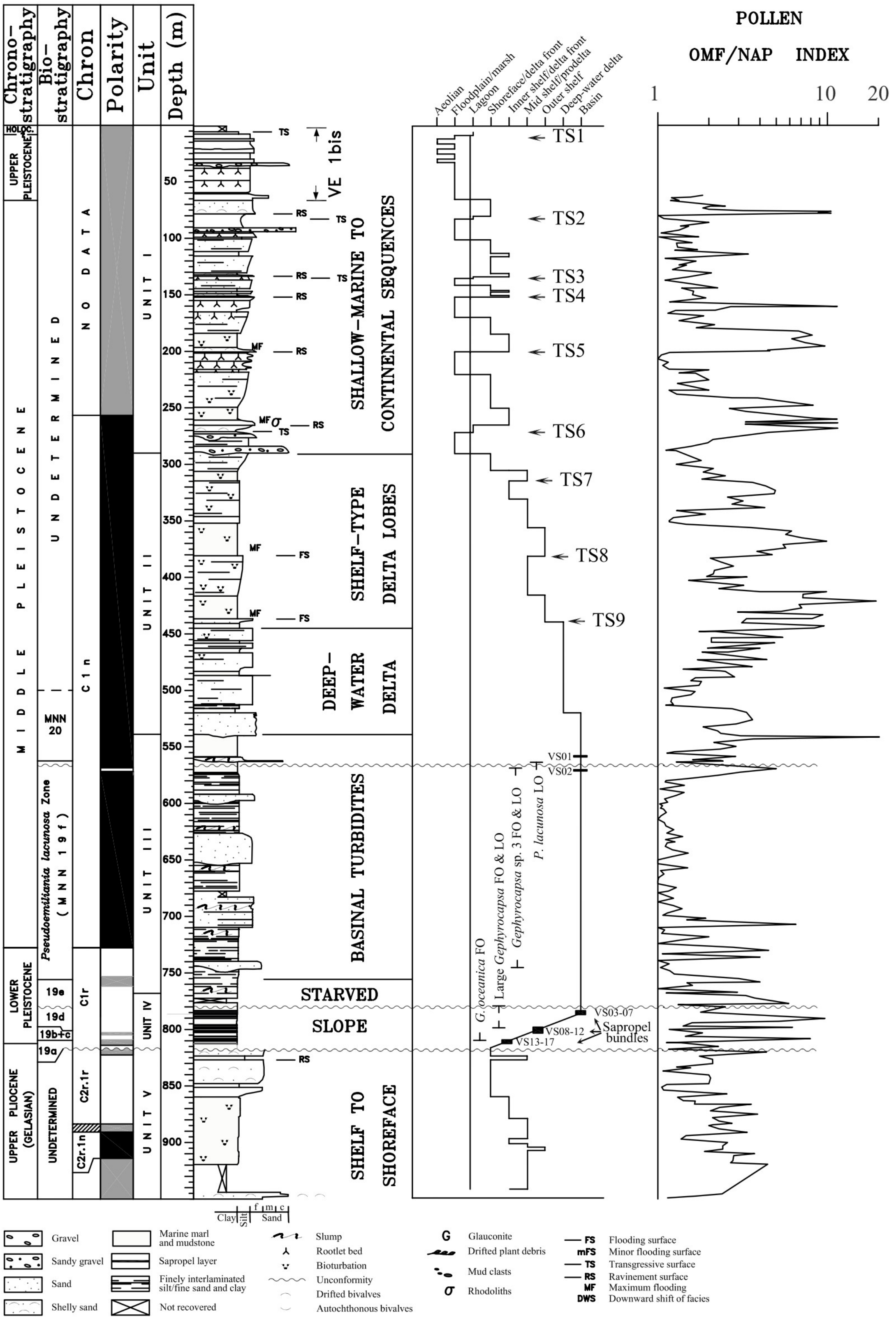

Figure 8: Stratigraphy of the succession recovered by VE-1 and VE-1bis cores (Massari et al., 2004).

The Holocene-Pleistocene limit is marked by a compacted clay layer known as "caranto" (*Figure 9*), which formed due to the dry climate during the final phase of the low sea level stand. The caranto layer tends to emerge on the mainland, varying between –5 and –23 meters in depth and gradually deepening towards the coast (Brambati et al., 2003). Early Holocene sediments are characterized by a discontinuous layer of silt and sand, often with a chaotic structure, mixed with shelly marine-lagoon sands. The middle-upper sections of this sedimentary sequence typically alternate between marine-lagoon deposits and floodplain sediments. During the subsequent high-stand sea level, alluvial sedimentation resumed along the outer northern and southern belts, corresponding to fluvial mouths. Additionally, some areas experienced episodes of emersion and submersion due to fluctuations in climate, changes in sediment sources, variations in subsidence rates, and human activities (Brambati et al., 2003).

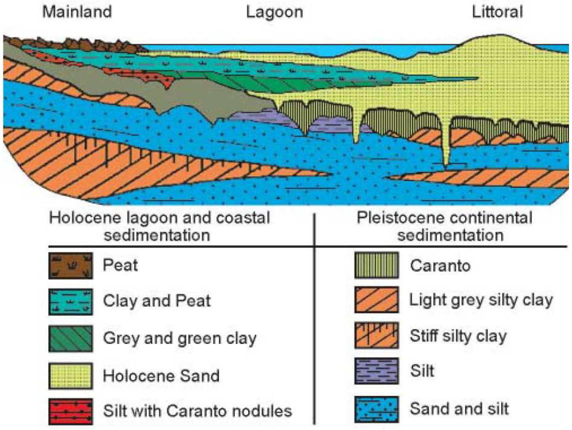

Figure 9: Holocene-Pleistocene stratigraphical sequence across the central lagoon of Venice (Gatto and Previatello, 1974).

A phenomenon that has particularly affected the Venice lagoon is subsidence, accelerated by intensive groundwater extraction in the 1950s and 1960s.

The term subsidence refers to any downward movement of the Earth's surface, regardless of the cause, the area affected, the rate of occurrence, the temporal evolution, or the resulting environmental changes. Subsidence is the final stage and the surface manifestation of a series of processes that occur underground and are, in some way, related to the geological or geomechanical structure of the area. Specific characteristics of the soil can either promote, accelerate, or inhibit these processes (Carbognin et al., 2011).

Subsidence occurs due to both natural and anthropogenic causes, which sometimes combine to produce the overall effect. Human activities often act as a "catalyst", significantly influencing the phenomenon, or as a "trigger," initiating it (Carbognin et al., 2011).

The main causes of natural subsidence can be attributed to deep tectonic processes (such as orogenetic movements, volcanic activity, and seismic activity), the lowering of the Pliocene substratum due to geostatic load (the weight of overlying sediments), chemical-physical transformations (diagenesis) of sediments due to lithostatic pressure, the natural compaction of unconsolidated sediments deposited on the Pliocene layer, and isostatic movements. Other minor and/or concurrent causes can include changes in the physical state, such as the natural drying of lake or lagoon basins, which leads to compaction and oxidation of organic materials. The most widespread form of anthropogenic subsidence, both in terms of extent and magnitude, is that induced by soil compaction resulting from the excessive extraction of underground fluids (Carbognin et al., 2011).

The subsidence caused by groundwater extraction in the lagoon area began around 1930, coinciding with the first settlements in Porto Marghera and the industrial exploitation of artesian aquifers. Initially, the use of these water resources was relatively modest, and the piezometric decline occurred slowly across the area until the late 1940s. However, with the post-war industrial boom in the 1950s and 1960s, the exploitation of the aquifer system became increasingly intense, affecting the six artesian aquifers that extend to a depth of 320 meters (Carbognin et al., 1998). Estimates of natural subsidence rates were derived from analyses of the VE-1 core, along with radiocarbon dating of late Pleistocene and Holocene sediments collected in the lagoon and coastal areas (Bortolami et al., 1986). Historically, human activities—from the diversion of tributaries to more recent excessive groundwater extraction—have reversed the natural evolutionary trend of the Venice lagoon, leading to its deepening and significantly altering its morphology. According to Brambati et al. (2003) and Kent et al. (2002), natural subsidence during the Quaternary period ranged between 0.5 and 1.3 mm/year, and 1950 and 1970 human-induced activities significantly increased this rate. Overall, there has been a relative elevation loss of 23 cm over the past century due to land subsidence (12 cm, of which 3 cm due to natural subsidence and 9 cm to anthropogenic subsidence) and rise in sea level (11 cm).

2.2 Seismic stations

Ambient noise was continuously recorded by two three-component receivers, respectively located on San Sèrvolo (*Figure 10*: Station A; 45°25’10.3"N 12°21’21.9"E) and Lido (*Figure 10*: Station B; 45°25’12.0"N 12°22’48.0"E) islands.

Figure 10: Location of station A (San Sèrvolo) and station B (Lido). - Image from Google Earth.

The receiver in San Sèrvolo, installed by the University of Padova, is a short band seismometer (*Tellus-5s*), with an acquisition frequency range of 0.2-100 Hz, a transduction factor of 400 V/m/s for the single ended version (S) and 800 V/m/s for the differential output (D), and a dynamic range $>$ 140 dB. The receiver in Lido, which belongs to the INGV Seismic Network 2Y (*AdriaArray Temporary Network: Italy – northeast*, station code A303A), is a symmetric triaxial *Trillium 120 PH* (*posthole*) seismometer, with an acquisition frequency range of 120 s - 150 Hz, a nominal sensitivity of 1200 V-s/m and a dynamic range of 168 dB at 1 Hz. The inter-stations distance was approximately 1870 m. The recording started on July 8th, 2023, and ended on October 28th, 2023.

3. Data Processing

The noise data processing divided into three main phases. The first phase was the cross-correlation of ZZ components with temporal stacking, and the measurement of the signal-to-noise ratio. The second phase focused on the measurement of the dispersion curve using the frequency–time analysis (FTAN). Finally, the third phase was the inversion of the dispersion curve to obtain the V_s and V_p ground profiles.

3.1 Cross-correlation

In the first phase of data processing, cross-correlation between the two stations was performed, obtaining a series of NCFs, one for each recording day, from July 8th, 2023 to October 28th, 2023. Cross-correlating long ambient noise sequences offered several advantages in terms of quality and reliability of the results. Firstly, it was expected that longer sequences would improve the signal-to-noise ratio (Bensen et al., 2007), increasing resolution and making coherent signals, like surface waves, more evident and easier to detect. Furthermore, it was expected that stacking more days of data would contribute also to increasing the reliability of the cross-correlation function (Bensen et al., 2007).

The whole process was done through a Python script, that included, prior to cross-correlation itself, the azimuth and distance calculation between the two seismic stations, respectively located in San Servolo (45.419521, 12.356072) and Lido (45.42, 12.38). This was done with `gps2dist_azimuth` function from `obspy.geodetics` library, which returns the distance between the stations and the azimuth, both needed to rotate the NE horizontal components into radial (R) and transverse (T) components.

The first parameter to be defined was the bandpass filter, which would allow frequencies within a specific range to pass through, while attenuating frequencies outside that range. Different frequency intervals were chosen between 0.1 Hz and 9 Hz, in order to evaluate which range would be the most representative of ambient noise in this case. After many tries, the optimal frequency range was found to be 0.1-5 Hz, where the significant amplitudes of the signal concentrated. A sliding time window of 3600 seconds (one hour) was then defined to segment the data before performing the cross-correlation. Subsequently, all the seismic traces were transformed from time domain to frequency domain using the Fast Fourier Transform (FFT) before applying a spectral whitening, used to improve the resolution and the appearance of seismic data by correcting for frequency attenuation. The seismic traces were sampled at a frequency of 20 Hz and, given the considerable duration of the seismic traces (each lasting 24 hours), they were shortened and defined within a time interval between -20 and +20 seconds, relative to the central time of the cross-correlation window, to focus on the most relevant portion of the signal.

Since the focus of this work was on Rayleigh waves, cross-correlation between the stations was finally performed, in the frequency domain, only considering the ZZ component of the traces. This process created a total of 111 noise correlation functions (NCFs), which were finally transformed back to the time domain through the Inverse Fast Fourier Transform (IFFT).

3.1.1 Temporal stacking

After the daily cross-correlations were returned to the time domain, they were added together (or ‘stacked’) using another Python code, representing in this way with a single function the entire recording period and improving the accuracy of the final cross-correlation function. In the NCF, the frequency range of the coherent noise and the length of the acquisition both depend on the distance between the receivers and on the frequency characteristics of the noise sources involved, like sea waves, shallow lagoon waves, traffic noise, wind, etc. (Boaga et al., 2010). The resulting correlation function computed between the stations (*Figure 11*) has a positive part and a negative part. The positive part refers to noise travelling from station A to station B, while the negative part from B to A. In the field of diffuse noise, the signal in both parts of the NCF is the same, causing the noise to travel in all directions (Boaga et al., 2010). When working with seismic traces with no preferred orientation and with low frequency seismic noise, like in this case, the same signal in both parts of NCF (symmetry conditions) assures that the inter-stations distance is appropriate (Boaga et al., 2007).

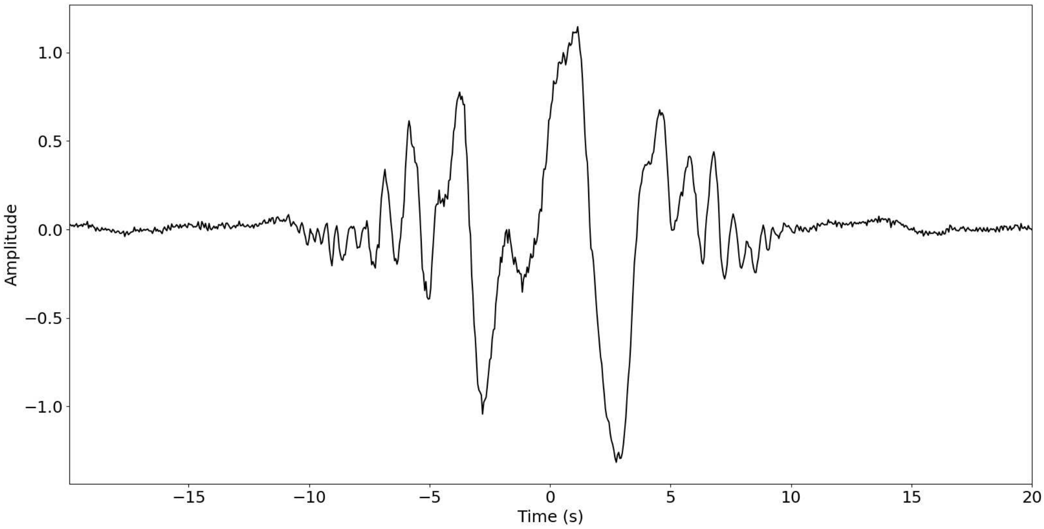

Figure 11: Result of the cross-correlation between the two stations, ZZ component. Two parts can be identified: the positive part, which represents the noise propagating from station A to station B (with A considered as the "master"), and the negative part, which represents the noise traveling from B to A (again with A as the reference).

Many authors, using the spatial reciprocity of the Green's function, average the positive and the negative parts of NCF, thereby imposing symmetry (i.e. Bensen et al., 2007). This procedure was followed also in this case: after the first stack, another one was done between the positive and the negative parts of the signal (*Figure 12*). Averaging them helped to reduce incoherent noise that may have affected one side of the correlation more than the other, since it constructively combined the information from both directions, reinforcing the coherent signal and better homogenizing the source distribution.

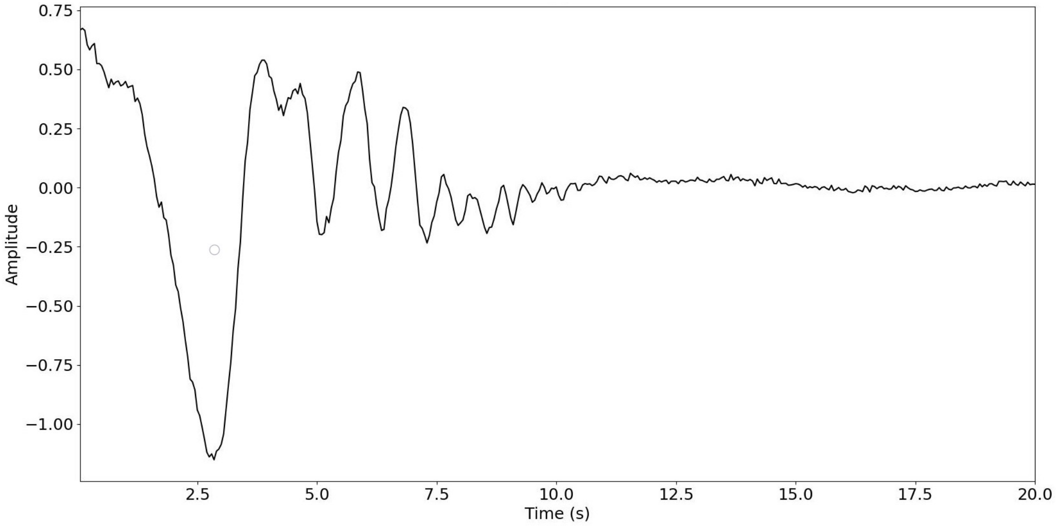

Figure 12: NCF after the final stack. The positive and negative parts were averaged, resulting in a single trace travelling in the positive direction.

3.1.2 Signal-to-noise ratio measurement

After the final stack (*Figure 12*), it was possible to measure the signal-to-noise ratio, defined as the ratio between the average signal amplitude and the average noise amplitude. The signal-to-noise ratio (SNR) indicates the quality of a signal with respect to the background noise. In other words, SNR quantifies how strong the signal is compared to the unwanted noise. In seismic data analysis, SNR is a critical parameter for determining the reliability and quality of the data.

Figure 13 shows the time windows used to measure the SNR: the interval representing the signal goes from 0 s to 10 s (blue lines), while the chosen interval associated with the background noise goes from 11 s to 20 s (red lines). Since the signal-to-noise ratio is able to indicate the quality of the overall signal, it was measured repeatedly to verify its general increase with progressively longer stacking periods, already demonstrated by Bensen et al. (2007). Moreover, the SNR was also measured before and after the application of the spectral whitening, in order to verify its effectiveness.

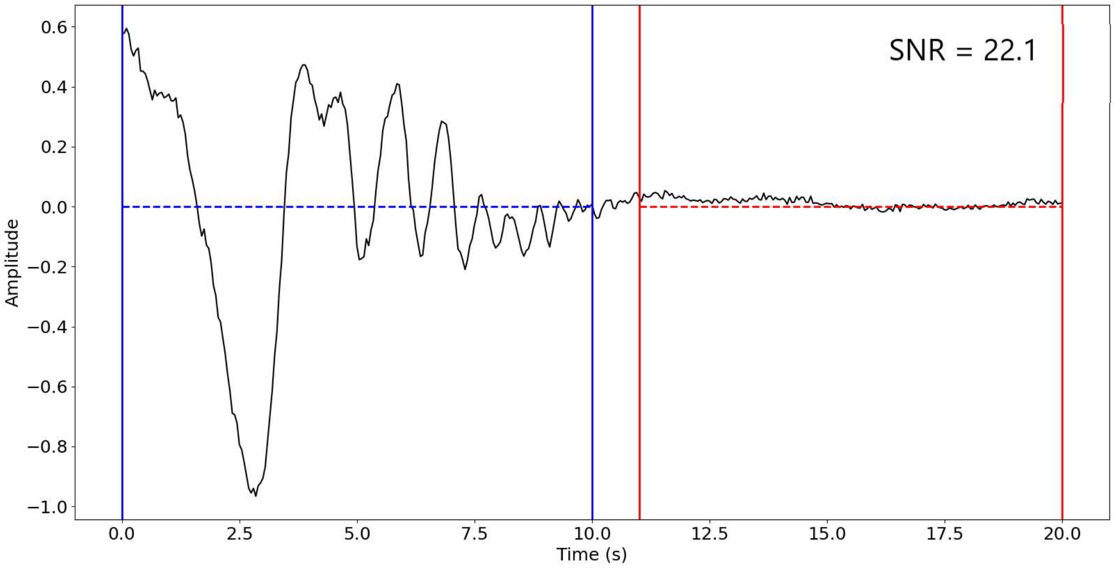

Figure 13: Example of how SNR measurements were obtained on the final 111-day cross-correlation, equivalent to approximately 16 weeks. Blue lines delineate the signal window, while red lines the noise window. SNR value is indicated at right-hand side of the image.

3.2 Frequency-Time Analysis

Surface waves are challenging to study, since they don't behave like regular harmonic waves. Their main characteristic, dispersion, can be described by a function rather than a single value, making them difficult to analyze in either time or spectral domain alone. To solve this, the final correlation function was processed using the Frequency-Time Analysis (FTAN), which separates signals based on their dispersion curve. This method employs a system of narrow-band Gaussian filters, with varying central frequency, that do not introduce phase distortion and give a good resolution in the time-frequency domain (Ndikum et al., 2014).

Imagine having a signal in the time domain, $W(t)$, and its corresponding Fourier transform in the frequency domain, $K(\omega)$. If the signal is passed through a series of narrow-band filters, with varying central frequency ω^H, the result will be a complex function of two variables (Romanelli, n.d.):

$$S\left(\omega^H, t\right) = \int_{-\infty}^{+\infty} H\left(\omega - \omega^H\right) K(\omega) e^{i\omega t} d\omega \tag{3.1}$$

The function $S(\omega^H, t)$ is not only determined by the original signal, but it involves also the filter characteristics. The choice of the filter $H(\omega - \omega^H)$ depends on the properties of the signal to be processed. When the shape of $H(\omega - \omega^H)$ is known, the functions $W(t)$

or $K(\omega)$ can be recovered (Romanelli, n.d.). $K(\omega)$ can be obtained from infinitesimally small filters ($\delta(\omega - \omega^H)$), while $W(t)$ from infinitely broad filters ($\frac{1}{\sqrt{2\pi}}$). For surface waves, the filter must not introduce phase distortion (H has to be real-valued) and it should give the best resolution. For these reasons, the optimal choice is a Gaussian filter (a filter whose impulse response is a Gaussian function), described by the central frequency ω^H and the width of the frequency band σ (Romanelli n.d.):

$$G(\omega) = \frac{1}{\sqrt{2\pi}\sigma} e^{\frac{-\omega^2}{2\sigma^2}} \tag{3.2}$$

Therefore, the result is a complex-valued function (Romanelli, n.d.):

$$S\left(\omega^H, t\right) = \frac{1}{\sqrt{2\pi}\sigma\left(\omega^H\right)} \int_{-\infty}^{+\infty} e^{-\frac{(\omega-\omega^H)^2}{2\sigma^2(\omega^H)}} K(\omega) e^{(i\omega t)} d\omega \tag{3.3}$$

Its graphical representation is the image of a matrix whose columns are the energy values at a certain period, and the rows are the energy values at constant group velocity (Ndikum et al., 2014). Converting the frequency to period and, given the epicentral distance, converting arrival times of energy packets to group velocity, the FTAN map of a signal is obtained (*Figure 14*), which is a contour map of $|S(\omega^H, t)|$. Finally, the dispersion curve of the signal, $\tau(\omega)$, is known approximately from FTAN results (Romanelli, n.d.).

Before running the Python code to perform the FTAN, different parameters had to be chosen. The inter-station distance needed to be specified (1870 m); the sampling interval (SI), considering a sampling frequency of 20 Hz, was set at 0.05 s, and the frequency and velocity intervals for the analysis were respectively set at 0.1-5 Hz and 80-2500 m/s. Finally, the alpha value, which governs the aperture of the Gaussian filter (the higher alpha, the narrower the bandpass), was chosen to be 10.

Firstly, the Python code computed the spectrum of the analytical signal by multiplying the signal spectrum by a Heaviside step function, to retain only the positive frequencies. Subsequently, the analytical signal was transformed into the frequency domain using the Fourier transform and the Gaussian filter was applied to isolate the spectral components within different frequency bands. At the end, an interactive colorimetric velocity-frequency graph, the FTAN map, was generated, where the dispersion curve could be manually or automatically picked (*Figure 14*).

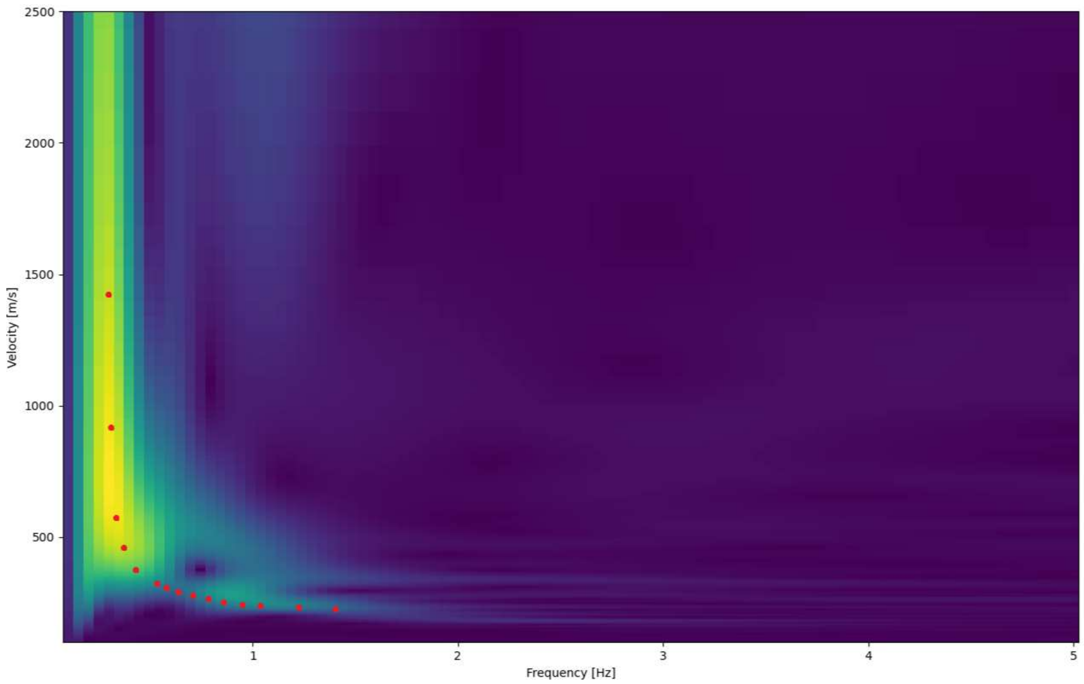

Figure 14: FTAN map and manual picking. The green-yellow "ridge", along which the picking of the Rayleigh wave fundamental mode dispersion curve was done, distributes along the frequencies where the energy is at its maximum.

In this work, the picking on the largest amplitudes was done manually, along the yellow-green "ridge" (Romanelli, n.d.), in order to extract the Rayleigh wave fundamental mode dispersion curve, around which the signal's energy focused.

After picking the dispersion curve, its points were extracted as a two-column matrix, containing the frequencies and the group velocities, respectively.

3.3 Inversion

Surface-wave inversion techniques allow to retrieve a layered velocity model of the subsurface from a dispersion curve. In this case, inversion was performed by using the “Surface Wave Inversion” environment in *Dinver*, a *Geopsy* tool, which performs a non-linear inversion with a Monte Carlo technique.

Firstly, the Rayleigh wave fundamental mode dispersion curve's parameters were imported as frequency (Hz) and group velocity values (m/s), previously retrieved through the FTAN, and the initial curve was displayed (*Figure 15*).

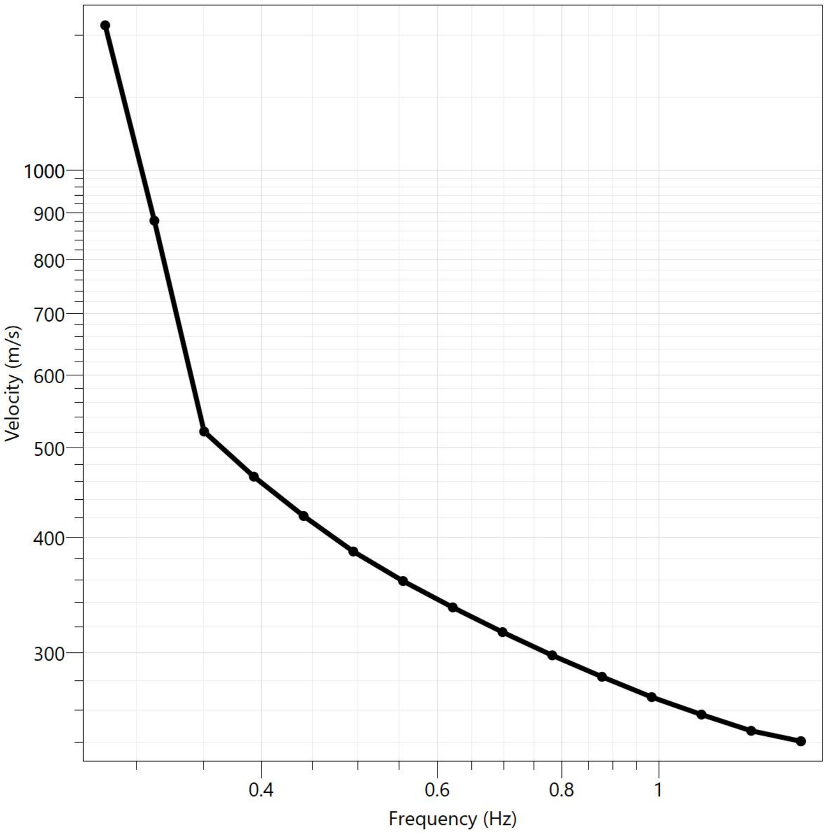

Figure 15: Dispersion curve obtained through the picking done through the FTAN.

In this inversion process, the unknown subsoil model was parametrized as a discrete function of depth, reaching 1500 m. In this approximation, the ground structure was modelled as a stack of five homogeneous isotropic layers – which should usually be limited to a maximum number of ten to keep the inversion computationally feasible –, each defined by five parameters: V_p, V_s, density, thickness and Poisson's ratio. Parameters were defined by a range of values or a fixed number, and were set to be either independent or dependent. In this case, S-wave velocities and thicknesses were chosen as independent parameters, while P-wave velocities, Poisson's ratios and densities were set as dependent on the previous two parameters, maintaining a fixed relationship with them.

For the first four layers, it was necessary to specify an estimated depth, assuming that their thickness increased going downwards. While, for the last layer, the software did not require setting a fixed depth. The reason is that the last layer is considered as a semi-infinite medium or an open boundary, whose thickness does not have an a priori defined limit. Through the inversion process, the software could then freely adapt the depth of the fifth layer depending on the observed data.

Finally, the S-wave velocity range values of each layer were chosen to be similar to the group velocities retrieved from the dispersion curve; the P-wave velocities were initially derived considering the relationship $V_p \approx \sqrt{3}V_s$, demonstrated in the first chapter, and, subsequently, they were significantly broadened, in order to ensure that the profile with the minimum misfit was both centered and consistent with the shear velocity model.
Table 1 below shows the initial parameters set for the inversion.

Layer	**Vp (m/s)**	**Vs (m/s)**	**Poisson's ratio**	**Density (kg/m^3)**	**Depth (m)**
1	200 - 900	100 - 300	0.2 - 0.5	1800	1 - 100
2	300 - 1500	150 - 500	0.2 - 0.5	1800	100 - 500
3	1000 - 3900	500 - 1300	0.2 - 0.5	1900	500 - 1000
4	1200 - 5400	600 - 1800	0.2 - 0.5	2000	1000 - 1400
5	3000 - 7500	1500 - 2500	0.2 - 0.5	2200	∞

Table 1: Initial parameters used for the inversion.

The inversion was then initiated, generating a large number of models around the parameter space. For each model, a forward calculation was performed to produce a theoretical group velocity dispersion curve, which was compared with the observed curve. A misfit function then quantified the difference between the two, and models with an acceptable fit were retained. Each model had a specific misfit value, ranging between 0.13 and 0.53 (*Figure 16*). The misfit is a quantitative measure of how well a proposed model matches the observed data. It essentially represents the difference between the observed data (i.e., the measured dispersion curve) and the data predicted by a model. The lower the misfit value, the better the model fits the observed data.

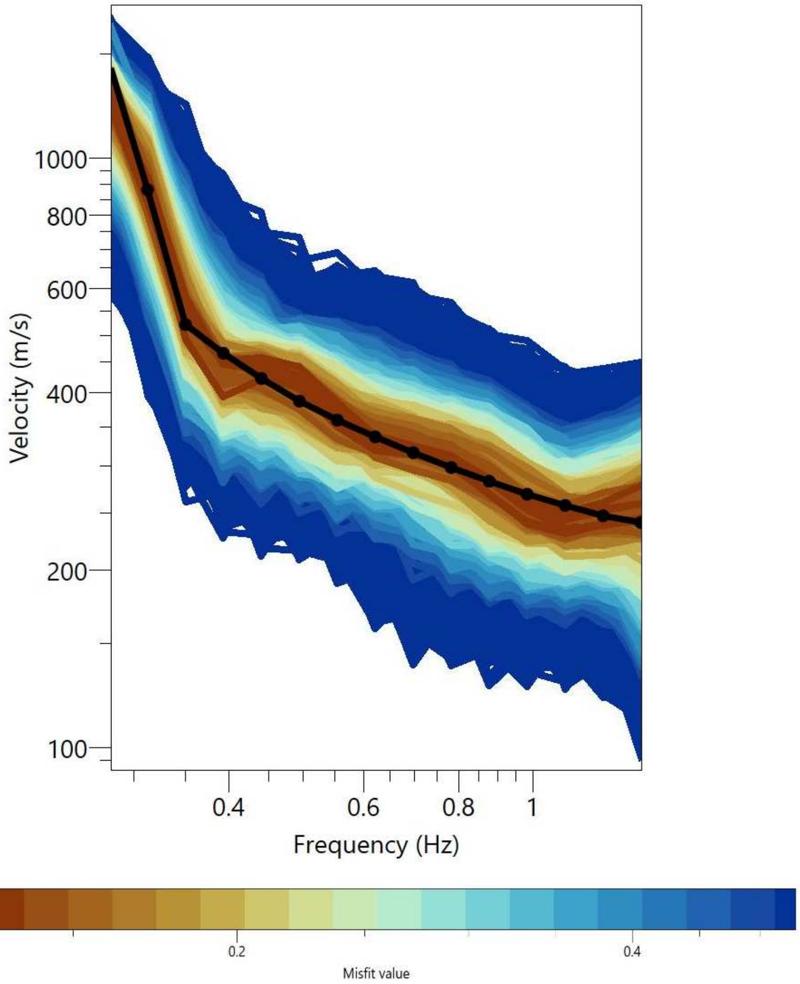

Figure 16: Dispersion curves generated around the initial model (black curve). Each color represents a different misfit value, ranging between 0.13 (dark red) and 0.53 (dark blue).

Together with the dispersion curves, the corresponding ground profiles for both V_s and V_p were finally generated (*Figure 17*). This type of inversion process helped explore the non-uniqueness of the solution by identifying multiple models that fitted the observed data. However, this method is computationally intensive, so it was crucial to balance the range of possible parameter values with practical constraints. Simplifying the model by reducing the number of layers or narrowing parameter ranges could make the process more efficient, but it had to be done carefully, since overly restricting the search may lead to missing viable solutions. Therefore, choosing the correct input parameters was indeed the most time-consuming part of the process, since the objective was to ensure that the theoretical curve and its respective initial subsoil profile were as representative and centered as possible compared to the models generated by the software.

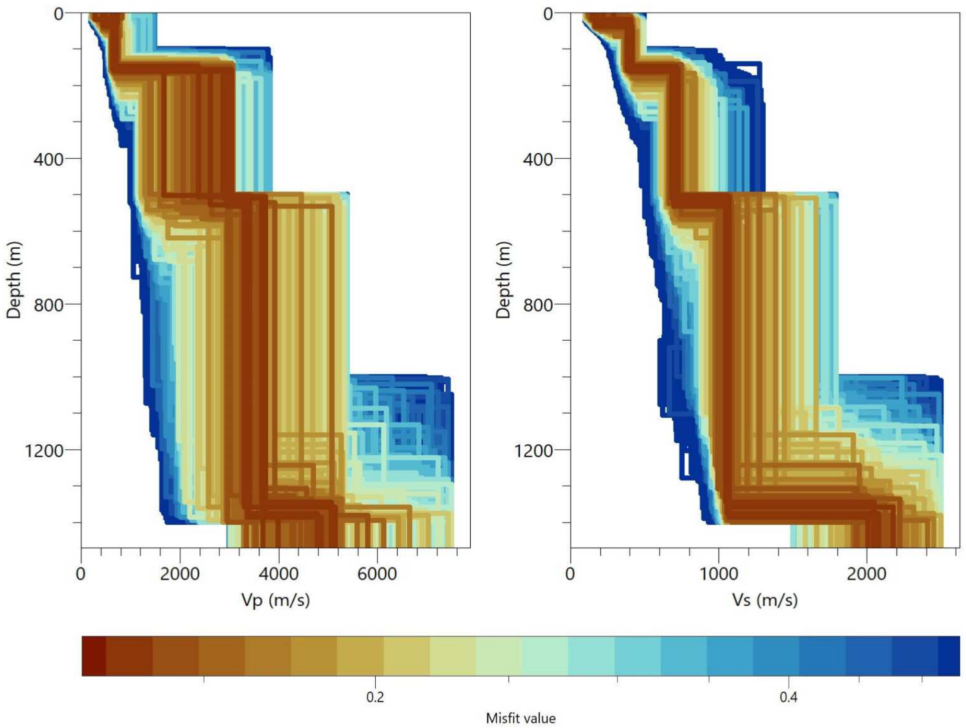

Figure 17: Vp and Vs profiles generated by the inversion. Each color represents a different misfit value, ranging between 0.13 (dark red) and 0.53 (dark blue).

At the end of the inversion process, all V_p and V_s profiles generated were exported as a .report file. The final compressional and shear velocity models were then obtained by extracting, through Windows PowerShell, the best profile, represented by the minimum misfit value.

4. Results

This chapter will present the final results, obtained through the extraction of the minimum misfit ground profile generated by the inversion. Moreover, it will discuss the outcomes derived from signal-to-noise ratio measurements.

4.1 Velocity models

The final deep velocity profiles were obtained by extracting the minimum misfit models through Windows PowerShell; subsequently they were imported and plotted in a .XLSX file. The results are shown in *Figure 18*: the minimum misfit models chosen can be identified in *Figure 17* among the dark red profiles. The error ranges were not inserted in the final plots, but they can be identified in *Figure 17*.

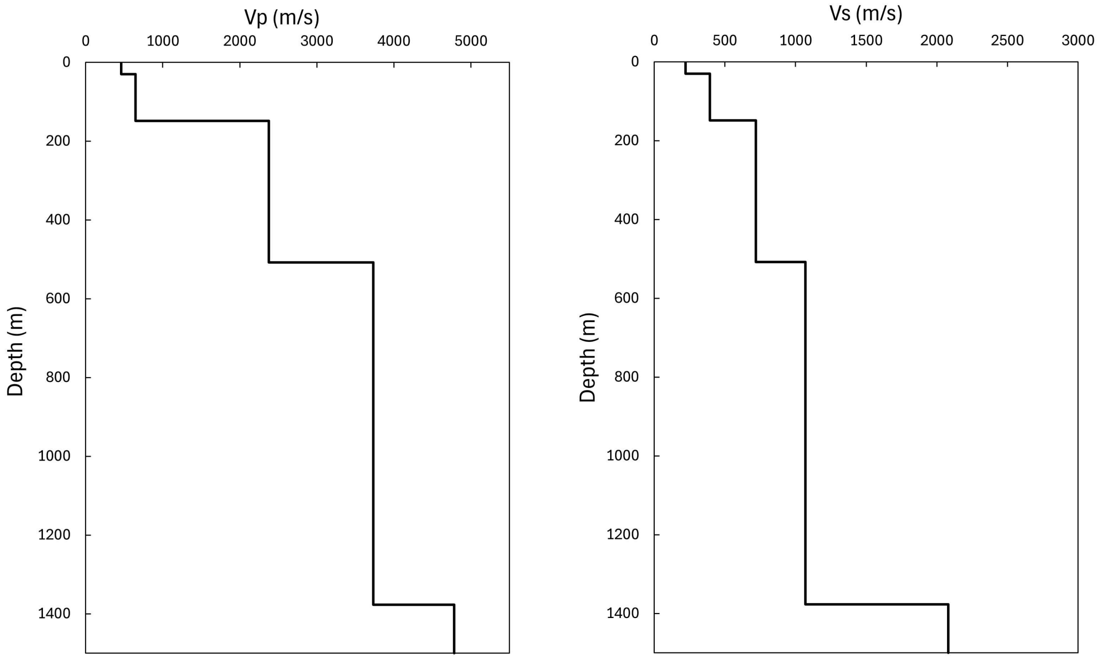

(a) (b)

Figure 18: Final deep compressional (a) and shear (b) wave velocity models chosen.

The velocity models obtained for the area between San Sèrvolo and Lido islands in the Venice lagoon show a stratified structure with five distinct layers, reaching a maximum depth visually limited in the final plots at 1500 meters.

The first layer, which is approximately 30 meters thick, is characterized by relatively low compressional and shear wave velocities (V_p of 461 m/s and V_s of 222 m/s), likely associated with unconsolidated surface sediments typical of the lagoon environment. The second layer, which extends down to approximately 148 meters, is characterized by higher velocities (V_p of 645 m/s and V_s of 394 m/s), indicative of greater sediment compaction. The third layer goes from 148 to 508 meters, with V_p and V_s velocities reaching 2377 and 719 m/s respectively, suggesting the presence of older, more compact geological units, possibly associated with cemented sand and gravel deposits or consolidated sedimentary rocks. The fourth layer extends from 508 to 1377 meters, with a V_p of 3731 m/s and a V_s of 1069 m/s. At approximately 1377 meters in depth, where the fifth layer begins, the shear velocity profile exhibits an abrupt increase, reaching 2080 m/s, while the compressional one shows a slower increase, up to 4784 m/s. This significant jump in velocities suggests the beginning of a much more rigid geological layer, with a quite different Poisson's ratio. *Table 2* below sums up the parameters characterizing each layer of the final model.

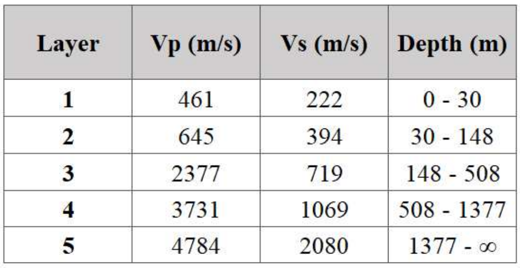

Layer	Vp (m/s)	Vs (m/s)	Depth (m)
1	461	222	0 - 30
2	645	394	30 - 148
3	2377	719	148 - 508
4	3731	1069	508 - 1377
5	4784	2080	1377 - ∞

Table 2: Parameters and layers in the final ground profiles.

Consulting the table of ground types classified based on their V_s in EN 1998-1:2004 (*Eurocode 8*), the first layer corresponds to a ground type C, characterized by an average shear wave velocity between 180 and 360 m/s, defined as 'deep deposits of dense or medium-dense sand, gravel or stiff clay (...).' The intermediate layers can be classified as type B, with an average V_s ranging between 360 m/s and 800 m/s, characterized by 'deposits of very dense sand, gravel, or very stiff clay, at least several tens of meters in thickness, with a gradual increase of mechanical properties with depth.' Finally, the last two layers are characterized by a V_s greater than 800 m/s, corresponding to a ground type A, which, in Italian and European seismic codes, is identified as the engineering bedrock.

4.2 Signal-to-noise ratio

The observations made by Bensen et al. (2007) regarding the improvement of the signal-to-noise ratio with increasing stacking periods were further validated by the results obtained in this work. *Figure 19* below shows the trend of the SNR measured on noise correlation functions obtained from progressively longer stacking periods. The most significant value is observed after stacking 10 weeks of data, where it reaches a peak of 22.8. After this, the SNR values fluctuate slightly between 22.0 and 22.8, reaching a value of 22.1 on the final NCF used to retrieve the dispersion curve (corresponding to 16 weeks of data). Additionally, the signal-to-noise ratio measured before applying the spectral whitening was at 16.5, lower if compared to 22.1 after spectral whitening.

These results confirm that stacking longer noise sequences and applying a spectral whitening effectively enhance the quality of the final correlation functions, as demonstrated by more stable and higher SNR values.

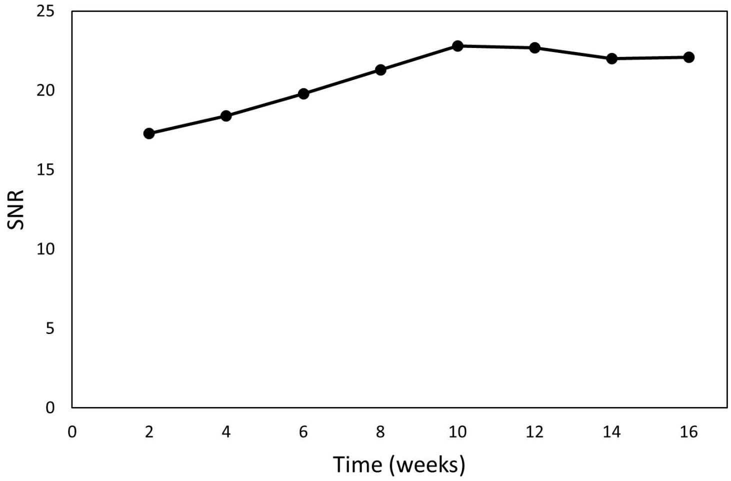

Figure 19: Signal-to-noise ratio measured for different stacking periods. The last value (22.1) was measured after a stack of 111 days of data (about 16 weeks), so it represents the SNR measured on final NCF. The shape of the curve shows how the SNR generally increases with progressively longer stacking periods.

5. Discussion

This chapter presents the results of this thesis, providing an interpretation and comparing them with existing studies conducted in similar geological settings to demonstrate their reliability.

In order to give an initial interpretation of the final velocity models, it is essential to consider the expected geology of the study area. So far, some information about the area's possible stratigraphy can be derived from the VE-1 and VE-1bis cores, previously discussed in the second chapter. Approximately at 4-5 km from the study area, the cores suggest that the stratigraphy in Tronchetto island presents some similarities with that expected in San Sèrvolo and Lido islands. Considering *Figure 8*, the layers seem to align with the velocity profiles, particularly at shallower depths. In the first 148 m, shear velocities range between 222 and 394 m/s, potentially representing the thin layers of sand, clay, silt, gravel, sandy gravel, and mudstone, stratigraphically identified in the top 160 m. As depth increases, between 148 m and 508 m, shear velocities are approximately 720 m/s, possibly due to the thickening of these layers and the presence, especially between 200-450 m, of mudstone and marine marl, whose V_s values can vary between 400 and 1000 m/s, depending on the marl's limestone/clay ratio. The same reasoning can be applied between 508 m and 1377 m, where the stratigraphy, especially after 815 m, shows thicker layers of marine marl, mudstone, and shelly sands. What needs to be noticed is that velocity profiles show a significant increase in seismic velocities after 1377 m, with a V_s slighltly overcoming 2000 m/s. Although sands, marls, and mudstones usually have lower shear velocities, they may be characterized by much higher velocities at greater depths, especially if they underwent lithification or significant porosity reduction.

To further assess the reliability of these velocity models, they were compared with findings from previous studies conducted in similar geological contexts.
A recent work by Boaga et al. (2010) used cross-correlation of seismic noise —sea noise and anthropic noise from an airport— to infer a 200 meters deep V_s structural model of the Venice Plain. After that, Mascandola et al. (2019) successfully reconstructed the V_s structure down to 1700 meters in Castelleone area (Cremona, Lombardy), aiming to map

the seismic bedrock in the Po Plain, a region with geological features similar to those of the Venice lagoon. More recently, Cascone et al. (2022) provided a detailed, shallow (30 meters) V_s structural model for two areas in the Po Plain, while deeper structures (up to 800 meters) were extrapolated using theoretical non-linear gradients from literature on deep alluvial basins. One of the investigated sites, located in the southern Po Plain, shares some geological features with Venice area, extending from gravel deposits to the Adriatic coast, with subsoil predominantly composed of silt and clay layers interspersed with sandy layers.

Comparing the results of this work with those of Boaga et al. (2010), several similarities in the V_s structural profiles emerge, despite some differences in the subdivision of the layers. Both studies report a V_s value of approximately 700 m/s at a depth of 200 meters. Additionally, at approximately 80-100 m, both studies show shear velocities oscillating around 400 m/s (*Figure 20*).

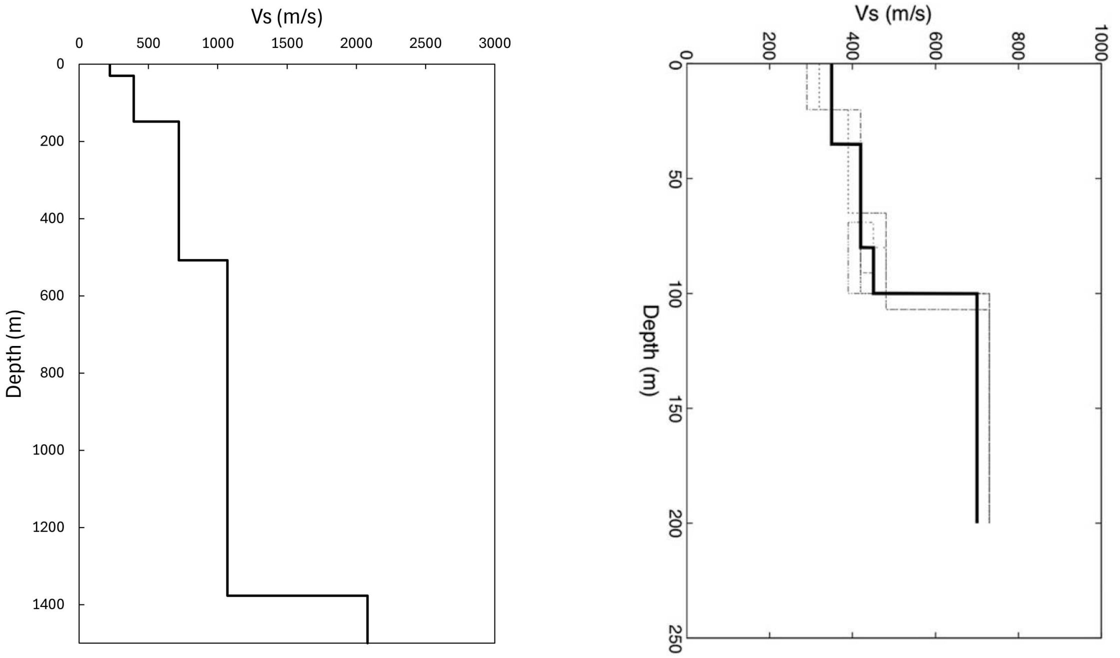

(a) (b)

Figure 20: Comparison between (a) the shear wave velocity profile obtained in this work and (b) the one obtained by Boaga et al. (2010).

The obtained velocity models can also be compared with those of Mascandola et al. (2019). Both studies identify, around 150-170 m in depth, a shear velocity increase, reaching 800-950 m/s in Mascandola et al.'s article, and 719 m/s in this study. Also, similar V_s values can still be found around 500 m in depth. Finally, an important increase in shear velocity is observed in both cases and at almost the same depths, around 1300 m. Depite the geographical distance between the considered locations, which are approximately 200 km apart, the profiles seem to align.

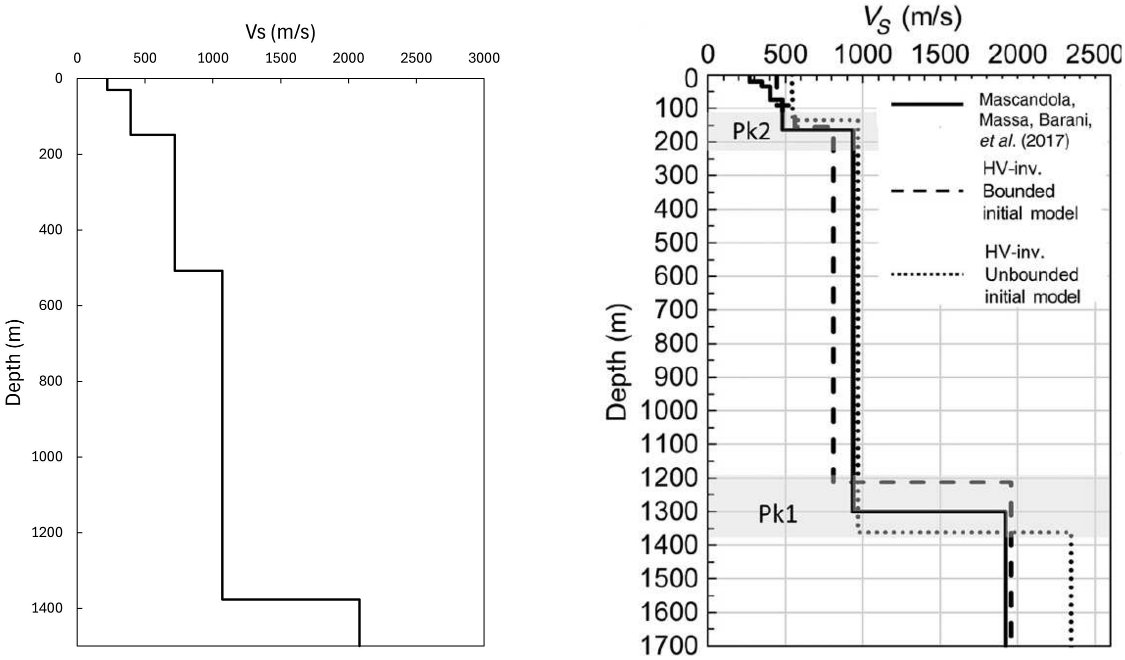

(a) (b)

Figure 21: Comparison between (a) the shear wave velocity profile obtained in this work and (b) the one obtained by Mascandola et al. (2019).

The results of this thesis also align with those by Cascone et al. (2022), particularly considering the similar sedimentary layers expected in Venice area. Cascone et al. identified a shear velocity of approximately 800 m/s at a depth of 400 meters (*Figure 22*), which is consistent with both the values obtained in this study and the ones identified by Mascandola et al (2019), at the same depth.

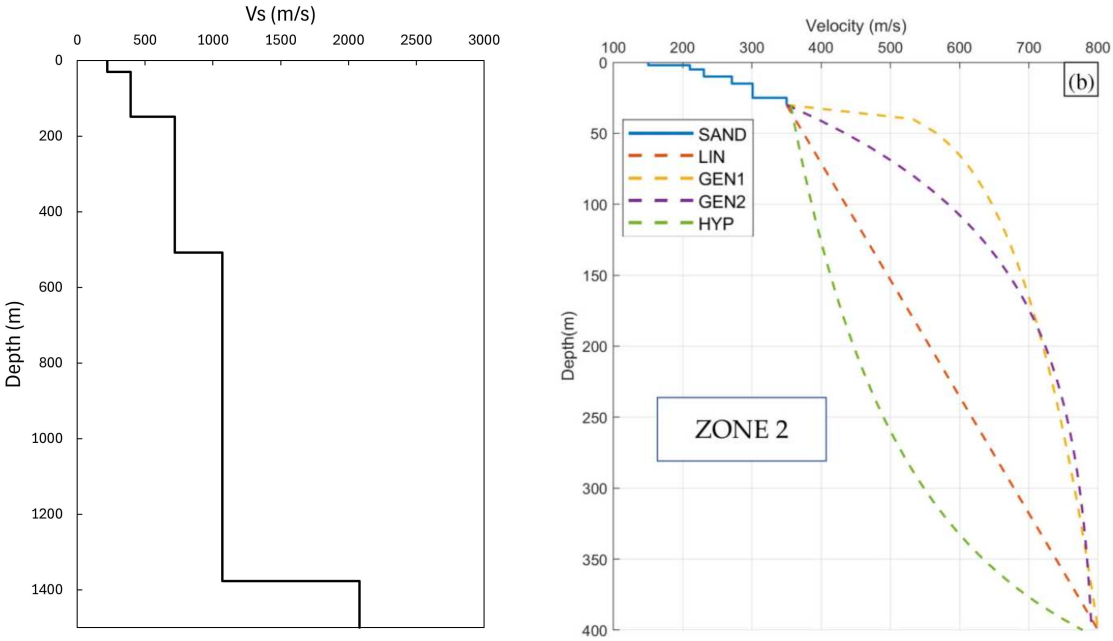

(a) (b)

Figure 22: Comparison between (a) the shear wave velocity profile obtained in this work and (b) the one obtained by Cascone et al. (2022).

Consulting the table of ground types classified by V_s values in EN 1998-1:2004 (*Eurocode 8*), the depth of 508 m —in this work— and 400 m —in Cascone et al. (2022)— can be therefore confirmed as the beginning of the engineering bedrock, defined by a 'rock or rock-like geological formation (...)', crucial to know for best assessing a site's seismic response and designing structures that can withstand seismic events.

6. Conclusions

This final chapter will draw the conclusions of this work, which aimed to determine the first deep shear wave model of the Venice lagoon using seismic noise interferometry.

The velocity models obtained in this study showed good consistency with the expected stratigraphy obtained from VE-1 and VE-1bis cores, especially within the first 148 meters, where they accurately reflect the presence of the thin layers of sand, clay, silt, gravel, and mudstone. At greater depths, below 1377 meters, the shear and compressional wave velocities overcome 2000 m/s and 4000 m/s respectively, suggesting that the mudstones, shelly sands and marine marls may have undergone lithification or porosity reduction, becoming more compact.

Comparing the obtained V_s models with those of other authors who investigated areas geologically similar to that of Venice, many similarities emerged. There is an alignment in the general trends and key depth intervals, such as the V_s values overcoming 800 m/s at about 400-508 meters, depths around which in this study, Cascone et al. (2022), and Mascandola et al. (2019) was identified the onset of the engineering bedrock.

Overall, the deep velocity models obtained are complessively consistent with the stratigraphy of the area —although further investigations may be necessary to delve deeper into the lithological characteristics at greater depths—, and they are also compatible with those obtained by Boaga et al. (2010), Mascandola et al. (2019) and Cascone et al. (2022), found in similar geological contexts. Therefore, the reliability of the deep velocity models obtained can be confirmed.

The results of the signal-to-noise ratio measurements confirmed what Bensen et al. (2007) had already demonstrated: stacking over increasingly long time-series generally improves the SNR ratio. In this study, it was also confirmed the effectiveness of the spectral whitening, which was able to improve the quality of the traces by enhancing the signal-to-noise ratio and balancing the frequency spectrum.

The deep shear wave velocity model obtained for the Venice lagoon will be of great importance for developing seismic shaking models, i.e. simulations of how seismic waves could propagate and influence the soil and structures in the historic center area. This is particularly relevant, because the historic center of Venice is an area of priceless cultural and architectural value, therefore characterized by high exposure and vulnerability to seismic events. Knowing the response of the ground to seismic activity allows to better predict the potential impact of an earthquake, and therefore to adopt more effective prevention measures, such as the seismic retrofitting or reinforcement of historic buildings.

References

[1] Achenbach, J. (2012). *Wave propagation in elastic solids*. Elsevier.

[2] Apatay, E. (2020). *Ambient Noise Seismic Interferometry Through Surface Seismic Data Acquisition vs Zero-Offset Vertical Seismic Profiling (VSP)* (Master's thesis, Michigan Technological University).

[3] Bensen, G. D., Ritzwoller, M. H., Barmin, M. P., Levshin, A. L., Lin, F., Moschetti, M. P., Yang, Y. (2007). Processing seismic ambient noise data to obtain reliable broad-band surface wave dispersion measurements. *Geophysical journal international,* 169(3), 1239-1260.

[4] Boaga, J., Iliceto, V., Vaccari, F., Panza, G.F. (2007). Shear-Wave Structural Model of Venetian Plane (Italy), from Seismic Noise measurements. *American Geophysical Union, Fall Meeting 2007, abstract NS11D-0797, 2007AGUFMNS11D0797B.*

[5] Boaga, J., Vaccari, F., Panza, G. F. (2010). Shear wave structural models of Venice Plain, Italy, from time cross correlation of seismic noise. *Engineering Geology*, 116(3-4), 189-195.

[6] Bortolami, G., Carbognin, L., Gatto, P. (1986). The natural subsidence in the Lagoon of Venice, Italy. *IAHS-AISH publication*, (151), 777-784.

[7] Braile, L. (2010). Seismic wave demonstrations and animations. *Purdue University*, 1-15.

[8] Brambati, A., Carbognin, L., Quaia, T., Teatini, P., Tosi, L. (2003). The Lagoon of Venice: geological setting, evolution and land subsidence. *Episodes Journal of International Geoscience*, 26(3), 264-268.

[9] Campillo, M., Roux, P., and Shapiro, N. M. (2011). Seismic, ambient noise correlation. *Encyclopedia of solid earth geophysics*, p-1230.

[10] Campillo, M., Roux, P., Romanowicz, B., Dziewonski, A. (2014). Seismic imaging and monitoring with ambient noise correlations. *Treatise on geophysics*, 1, 256-271.

[11] Carbognin, L., Teatini, P., Tosi, L., Strozzi, T., Vitturi, A., Mazzuccato, A. (2011). Subsidenza. In *Atlante Geologico della Provincia di Venezia. Note Illustrative*. Provincia di Venezia

[12] Carbognin, L., Tosi, L. (1998). La subsidenza nell'area veneziana: attuali tendenze ed implicazioni. *GEOfluid 98-Problemi di Geoingegneria: Estrazioni di Fluidi e Subsidenza*

[13] Cascone, V., Barone, I., Boaga, J. (2022). Velocity gradients choice affecting seismic site response in deep alluvial basins: Application to the Venetian Plain (Northern Italy). *Journal of Geophysics and Engineering*, 19(1), 1-13.

[14] Chen, Y., Saygin, E. (2020). Empirical Green's function retrieval using ambient noise source-receiver interferometry. *Journal of Geophysical Research: Solid Earth*, 125(2), e2019JB018261.

[15] Curtis, A., Gerstoft, P., Sato, H., Snieder, R., Wapenaar, K. (2006). Seismic interferometry—turning noise into signal. *The Leading Edge*, 25(9), 1082-1092.

[16] Dal Moro, G. (2014). *Surface wave analysis for near surface applications*. Elsevier.

[17] Damiano Pesaresi, Giuliana Rossi. (2022). *AdriaArray Temporary Network: Italy - northeast* [Data set]. *International Federation of Digital Seismograph Networks*. Retrieved from: `https://doi.org/10.7914/1P36-6T87`

[18] Derode, A., Larose, E., Tanter, M., De Rosny, J., Tourin, A., Campillo, M., Fink, M. (2008). Recovering the Green's function from field-field correlations in an open scattering medium (L).

[19] Foti, S., Lai, C. G., Rix, G. J., Strobbia, C. (2014). *Surface wave methods for near-surface site characterization*. CRC press.

[20] Frascari, A. (2014). Qualitative mapping and characterization of saltwater intrusion in channels and rivers of the Venice lagoon, Southern basin.

[21] Gatto, P., Previatello, P. (1974). *Significato stratigrafico, comportamento meccanico e distribuzione nella laguna di Venezia di una argilla sovraconsolidata*

nota come "caranto": TR 70. CNR, Laboratorio per lo studio della dinamica delle grandi masse.

[22] Hara, M. T., Yokoi, T., Sugahara, M. *Application of seismic interferometry to broadband ambient noise recordings in and around the Philippines islands.*

[23] Kent, D. V., Rio, D., Massari, F., Kukla, G., Lanci, L. (2002). Emergence of Venice during the Pleistocene. *Quaternary Science Reviews*, 21(14-15), 1719-1727.

[24] Laske, G., and R. Widmer-Schnidrig. (2015). *Theory and observations: Normal mode and surface wave observations.*

[25] Mascandola, C., Massa, M., Barani, S., Albarello, D., Lovati, S., Martelli, L., Poggi, V. (2019). Mapping the seismic bedrock of the Po Plain (Italy) through ambient-vibration monitoring. *Bulletin of the Seismological Society of America*, 109(1), 164-177.

[26] Massari, F., Rio, D., Barbero, R. S., Asioli, A., Capraro, L., Fornaciari, E., Vergerio, P. P. (2004). The environment of Venice area in the past two million years. *Palaeogeography, Palaeoclimatology, Palaeoecology*, 202(3-4), 273-308.

[27] Muhumuza, K. (2016). *The use of seismic interferometry to study Earth structure variations in the Antarctica.*

[28] Nishida, K. (2017). Ambient seismic wave field. *Proceedings of the Japan Academy, Series B*, 93(7), 423-448.

[29] Ndikum, E. N., Tabod, C. T., Tokam, A. P. K. (2014). Frequency time analysis (FTAN) and moment tensor inversion solutions from short period surface waves in Cameroon (Central Africa). *Open Journal of Geology, 2014.*

[30] Romanelli, F. (n.d.). FTAN analysis [PowerPoint slides]. *Theoretical Seismology, Astrophysics and Cosmology, and Earth and Environmental Physics* Course, University of Trieste.

[31] Shapiro, N. M., Campillo, M., Stehly, L., Ritzwoller, M. H. (2005). High-resolution surface-wave tomography from ambient seismic noise. *Science*, 307(5715), 1615-1618.

[32] Shearer, P. M. (2009). *Introduction to Seismology*, Cambridge University Press.

[33] Snieder, R., Wapenaar, K. (2010). Imaging with ambient noise. *Physics Today*, 63(9), 44-49.

[34] Standard, B. (2005). Eurocode 8: Design of structures for earthquake resistance. *Part, 1,* 1998-1.

[35] Tosi, L., Rizzetto, F., Bonardi, M., Donnici, S., Serandrei Barbero, R., Toffoletto, F. (2007). Note illustrative della carta geologica d'italia alla scala 1: 50.000 foglio 128 venezia.

[36] Wapenaar, K. (2004). Retrieving the elastodynamic green's function of an arbitrary inhomogeneous medium by cross correlation. *Phys. Rev. Lett.*, 93(25):254301.

[37] Wapenaar, K., Draganov, D., Snieder, R., Campman, X., Verdel, A. (2010). Seismic Interferometry: Tutorial on seismic interferometry: Part 1—Basic principles and applications.

Links:

1. `https://lunitek.it/seismic/seismic-sensors/tellus-5s/`
2. `https://terremoti.ingv.it/en/instruments/network/2Y`
3. `https://www.geological-digressions.com/wp-content/uploads/2017/04/earthquake-seismogram.jpg?ssl=1`

Appendix: codes

The following Python code was used to apply the bandpass filter and the spectral whitening, perform the cross-correlation and do the stack of all the traces to obtain the noise correlation function between the stations. Written by Piero Poli and Ilaria Barone; modified by Silvia De Marchi.

```
#!/usr/bin/env python3
# -*- coding: utf-8 -*-
"""
Created on Mon Oct 30 14:10:04 2023

@author: pieropoli, Ilaria
"""
import glob
import matplotlib.pyplot as plt
from obspy import read, read_inventory
import numpy as np
from datetime import datetime, timedelta
from pipy import xcorr
from obspy.geodetics import gps2dist_azimuth
import os
from noise import noisecorr

dd = gps2dist_azimuth(45.42,12.38,45.419521,12.356072)

# paramters
outdir = 'C:\\Users\\HUAWEI\\Desktop\\Università\\tesi\\corr_fb\\'

fb1=0.1
fb2=5
win=3600

outdir = outdir + 'corr_fb' + str(fb1) + str(fb2)

if os.path.exists(outdir) == False:
    os.mkdir(outdir)
# Specify the start and end dates
```

```
start_date = datetime(2023, 7, 8)
end_date = datetime(2023, 10, 28)

# Initialize an empty list to store the formatted strings
date_strings = []

# Generate strings in the specified format and append to the list
current_date = start_date
while current_date <= end_date:
    formatted_date = current_date.strftime('%Y-%m-%dT%H%M%S.000000Z')
    date_strings.append(formatted_date)
    current_date += timedelta(days=1)

XCORR_ALL = []
for ist in date_strings:
    folder = 'Dati_Venezia_SanServolo_20Hz/*' + ist[0:10] + '*.mseed'
    files = glob.glob(folder)

    folder2 = 'Dati_Venezia_lido_20Hz/*' + ist[0:10] + '*.mseed'
    files2 = glob.glob(folder2)

    if len(files) == 3 and len(files2) == 3:

        st_igor=read(folder)
        st_igor.filter('bandpass',freqmin=fb1,freqmax=fb2)


        st_igor.rotate(method='NE->RT',back_azimuth=dd[1])

        st_lido=read(folder2)
        st_lido.filter('bandpass',freqmin=fb1,freqmax=fb2)

        st_lido.rotate(method='NE->RT',back_azimuth=dd[1])

        t = st_igor[0].times('timestamp')
        fs=st_igor[0].stats.sampling_rate

        t0=st_igor[0].stats.starttime

        print(t0)

        # Use noisecorr for cross-correlation in the frequency domain
        _, SUMCORR = noisecorr(st_igor[2], st_lido[2], window_length=win)
        XCORR = np.fft.fftshift(np.fft.irfft(SUMCORR))
        SI = 1 / fs
        time = np.arange(0, len(XCORR) * SI, SI) - (len(XCORR) * SI / 2)
```

```
        ft = np.where((time>-20) & (time<20))[0]
        tcorr = time[ft]
        XCORR2 = XCORR[ft]

        #plt.figure()
        #plt.plot(tcorr,XCORR2)

        XCORR_ALL.append(XCORR2)

# I save the daily cross-correlations
nameout = os.path.join(outdir, 'dailycorr_fb' + str(fb1) +
  '_' + str(fb2) + '_zz.npz')
np.savez(nameout,c=XCORR_ALL,fs=fs,tcorr=tcorr)
print('save corr for ' + str(t0))

# Stack of all days
XCORR_STACK = np.sum(np.array(XCORR_ALL),0)
plt.figure()
plt.plot(tcorr,XCORR_STACK, color='black')
plt.xlabel('Time (s)', fontsize=18)
plt.ylabel('Amplitude', fontsize=18)
plt.title('ZZ', fontsize=18)
plt.gca().tick_params(axis='x', labelsize=18)
plt.gca().tick_params(axis='y', labelsize=18)

# I save the stack of all daily cross-correlations
nameout = os.path.join(outdir, 'stackcorr_fb' + str(fb1) +
  '_' + str(fb2) + '_zz.npz')
np.savez(nameout,c=XCORR_STACK,fs=fs,tcorr=tcorr)
```

The following Python code was used to do the average of the negative and positive parts of the correlation function. Written by Silvia De Marchi.

```
# -*- coding: utf-8 -*-
"""
Created on Wed Jun 5 15:30:00 2024
@author: Silvia
"""

import os
import numpy as np
import matplotlib.pyplot as plt

# Define the path to the stacked correlation file
```

```
stacked_corr_file = 'C:\\Users\\HUAWEI\\Desktop\\Università\\tesi
  \\stackcorr_fb0.1_5.0_zz.npz'

# Load the stacked correlation data
data = np.load(stacked_corr_file)
XCORR_STACK = data['c']
tcorr = data['tcorr']
fs = data['fs']

# Process the trace to have only positive times
# Separate positive and negative times
positive_indices = tcorr >= 0
negative_indices = tcorr < 0

# Flip the negative part to make it positive
flipped_negative_trace = np.flip(XCORR_STACK[negative_indices])

# Ensure the positive trace and flipped negative trace have the same length
min_length = min(len(flipped_negative_trace), len(XCORR_STACK[positive_indices]))
positive_trace = XCORR_STACK[positive_indices][:min_length]
flipped_negative_trace = flipped_negative_trace[:min_length]

# Compute the average of the positive and flipped negative traces
averaged_trace = (positive_trace + flipped_negative_trace) / 2

# Save the processed trace to a new .npz file
output_directory = 'C:\\Users\\HUAWEI\\Desktop\\Università\\tesi\\0.1_5_zz'
os.makedirs(output_directory, exist_ok=True)
averaged_filename = os.path.join(output_directory,
  'averaged_stackcorr_fb0.1_5.0_zz.npz')
np.savez(averaged_filename, averaged_trace=averaged_trace,
  tcorr=tcorr[positive_indices][:min_length], fs=fs)
print(f'Saved averaged correlation as {averaged_filename}')

# Plot the averaged trace
plt.figure()
plt.plot(tcorr[positive_indices][:min_length], averaged_trace, color='black')
plt.xlabel('Time (s)', fontsize=18)
plt.ylabel('Amplitude', fontsize=18)
plt.title('Averaged Component: zz', fontsize=18)
plt.gca().tick_params(axis='x', labelsize=18)
plt.gca().tick_params(axis='y', labelsize=18)
plt.xlim(np.min(tcorr[positive_indices][:min_length]),
  np.max(tcorr[positive_indices][:min_length]))
plt.show()
```

The following Python code was used to measure the signal-to-noise ratio. Written by Silvia De Marchi.

```
# -*- coding: utf-8 -*-
"""
Created on Mon Oct 30 14:10:04 2023

@author: Silvia
"""

import numpy as np

# Define the path
npz_file_path = 'C:\\Users\\HUAWEI\\Desktop\\Università\\tesi\\
  averaged_stackcorr_fb0.1_5.0_zz.npz'

# Upload file
data = np.load(npz_file_path)

# Extract trace (stackcorr) and sampling frequency (fs)
trace = data['averaged_trace'].flatten()
fs = data['fs']
tcorr = data['tcorr']

# Define time intervals for signal and noise (in seconds)
signal_interval = (0, 10)
noise_interval = (11, 20)

# Find the corresponding time intervals of signal and noise
signal_indices = np.where((tcorr >= signal_interval[0]) &
   (tcorr <= signal_interval[1]))[0]
noise_indices = np.where((tcorr >= noise_interval[0]) &
   (tcorr <= noise_interval[1]))[0]

if len(signal_indices) == 0 or len(noise_indices) == 0:
    print("Signal or noise range not found.")
else:
    # Extract the signal and noise portions of the track
    signal = trace[signal_indices]
    noise = trace[noise_indices]

    # Measures the amplitude of the signal and noise in the specified range
    signal_amplitude = np.max(signal) - np.min(signal)
    noise_amplitude = np.max(noise) - np.min(noise)
```

```
    # Measure the signal-to-noise ratio (SNR)
    snr = signal_amplitude / noise_amplitude

    print("Signal Amplitude:", signal_amplitude)
    print("Noise Amplitude:", noise_amplitude)
    print("Signal-to-noise Ratio:", snr)
```

The following Python code was used for the Frequency-Time Analysis. Written by Ilaria Barone, modified by Silvia De Marchi.

```
# -*- coding: utf-8 -*-
"""
Created on Fri Sep 22 13:53:50 2023

@author: Ilaria

"""

import numpy as np
import matplotlib.pyplot as plt

# Load the trace from the .npz file
file_path = 'C:\\Users\\HUAWEI\\Desktop\\Università\\tesi\\
  averaged_stackcorr_fb0.1_5.0_zz.npz'
data = np.load(file_path)
trace = data['averaged_trace']

def FTAN(trace, SI, dist, alpha, fix, fmin, fmax, vmin, vmax):

"""
Function to perform the frequency-time analysis for a
single trace, producing a velocity/frequency plot
"""

    # 1) Compute spectrum of analytical signal.
    L = len(trace)
    time = np.arange(0, SI * len(trace), SI)
    NFFT = 2 ** int(np.ceil(np.log2(L)))
    S = np.fft.fftshift(np.fft.fft(trace, NFFT))
    SR = 1/SI
    freq = np.linspace(-SR / 2, SR / 2 - SR / NFFT, NFFT)
    Sa = S * (2 * (freq >= 0))  # Apply Heaviside step
      function to keep the positive frequencies
```

```
    # 2) Loop on frequency and FT spectrum computation
      (as in Bensen et al., 2007)
    freqs_FT = np.linspace(fmin, fmax, 100)
    if fix == 0:
        alpha = alpha*(dist/1000)
    FTSpec = np.empty((L, len(freqs_FT)))
    for f in range(len(freqs_FT)):
        G = np.exp(-alpha * ((freq - freqs_FT[f]) / freqs_FT[f]) ** 2)
        Sa_filt = Sa * G
        trace_f = np.fft.ifft(np.fft.fftshift(Sa_filt), NFFT)
        FTSpec[:, f] = np.abs(trace_f[:L])

    vel = dist / time
    F, V = np.meshgrid(freqs_FT, vel[1:])
    plt.figure()
    plt.pcolormesh(F, V, FTSpec[1:,:])
    plt.colorbar()
    plt.xlabel('Frequency [Hz]')
    plt.ylabel('Velocity [m/s]')
    plt.ylim(vmin, vmax)
    #plt.xscale('log')
    plt.show()

    # 3) Picking of dispersion curve
    # press ENTER when finish picking
    print("Click on the max amplitudes {}:")
    c_max = plt.ginput(-1, timeout=0)
    c_max = np.array(c_max)

    return FTSpec,F,V,c_max

# Parameters for the FTAN function call
SI = 0.05  # Sampling interval [s] , having a sampling frequency of 20 Hz
dist = 1870  # Distance [m]
alpha = 10
fix = 1  # Fixed alpha
fmin = 0.1  # Minimum frequency [Hz]
fmax = 5  # Maximum frequency [Hz]
vmin = 80  # Minimum velocity [m/s]
vmax = 2500 #Maximum velocity [m/s]


# Run the FTAN function
FTSpec, F, V, c_max = FTAN(trace, SI, dist, alpha, fix, fmin, fmax, vmin, vmax)
```

Acknowledgements

Vorrei innanzitutto ringraziare il Prof. Boaga, il Prof. Poli e la Dott.ssa Ilaria Barone, il cui prezioso supporto è stato fondamentale per la realizzazione di questa tesi.

Ringrazio tutte le persone che hanno fatto e che fanno ancora parte della mia vita. Anche se meno di altre, avete comunque lasciato qualcosa.

Ringrazio in particolar modo miei genitori, per aver sempre creduto in me e per avermi sostenuta durante questo percorso, economicamente ed emotivamente. Senza di voi niente di tutto questo sarebbe stato possibile.

Ringrazio Erika, Lorisa, Sofia, Silvia e Jelena, sempre vicine anche quando distanti. Mi avete sempre strappato un sorriso nei momenti difficili e mi avete motivata a dare sempre il meglio di me. È passato letteralmente un decennio, eppure siamo ancora qui insieme.

Ringrazio Emma, che dal primissimo giorno di università, quasi cinque anni fa, è entrata nella mia vita e non ne è più uscita. Hai riso con me nei momenti belli, e mi hai ascoltata e consolata in quelli più brutti. Senza di te non sarei arrivata fin qui tutta intera (o quasi).

Ringrazio Vanessa, Lucrezia ed Emily, che sono improvvisamente rientrate a far parte della mia vita dopo tanti anni. Stare con voi mi fa tornare bambina, quando l'unica preoccupazione era trovare il coraggio per far firmare una nota.

Infine, ringrazio Gian, la mia metà. Mi hai ascoltata, aiutata e amata in ogni istante, sostenendomi ad ogni passo e credendo sempre in me. Nonostante la distanza e le difficoltà che ha portato, mi sei sempre stato vicino, perché in realtà ogni giorno mi hai tenuta per mano.